

## Article

# Ultra-High Contrast MRI: Using Divided Subtracted Inversion Recovery (dSIR) and Divided Echo Subtraction (dES) Sequences to Study the Brain and Musculoskeletal System

Daniel Cornfeld <sup>1,2,3,\*</sup>, Paul Condron <sup>1,2</sup>, Gil Newburn <sup>1</sup>, Josh McGeown <sup>1</sup>, Miriam Scadeng <sup>2</sup>, Mark Bydder <sup>1</sup>, Mark Griffin <sup>1,4</sup>, Geoffrey Handsfield <sup>5</sup>, Meeghage Randika Perera <sup>5</sup>, Tracy Melzer <sup>6,7</sup>, Samantha Holdsworth <sup>1,2</sup>, Eryn Kwon <sup>1,5</sup> and Graeme Bydder <sup>1,8</sup>

<sup>1</sup> Mātai Medical Research Institute, Tairāwhiti Gisborne 4010, New Zealand

<sup>2</sup> Department of Anatomy and Medical Imaging—Faculty of Medical and Health Sciences & Centre for Brain Research, University of Auckland, Auckland 1010, New Zealand

<sup>3</sup> Te Whatu Ora Tairāwhiti, Gisborne 4010, New Zealand

<sup>4</sup> Insight Research Services Associated, Gold Coast 4215, Australia

<sup>5</sup> Auckland Bioengineering Institute, University of Auckland, Auckland 1010, New Zealand

<sup>6</sup> Department of Medicine, University of Otago, Christchurch 8011, New Zealand

<sup>7</sup> New Zealand Brain Research Institute, Christchurch 8011, New Zealand

<sup>8</sup> Department of Radiology, University of California, San Diego, CA 92093, USA

\* Correspondence: d.cornfeld@matai.org.nz

**Abstract:** Divided and subtracted MRI is a novel imaging processing technique, where the difference of two images is divided by their sum. When the sequence parameters are chosen properly, this results in images with a high  $T_1$  or  $T_2$  weighting over a small range of tissues with specific  $T_1$  and  $T_2$  values. In the  $T_1$  domain, we describe the implementation of the divided Subtracted Inversion Recovery Sequence (dSIR), which is used to image very small changes in  $T_1$  from normal in white matter. dSIR has shown widespread changes in otherwise normal-appearing white matter in patients suffering from mild traumatic brain injury (mTBI), substance abuse, and ischemic leukoencephalopathy. It can also be targeted to measure small changes in  $T_1$  from normal in other tissues. In the  $T_2$  domain, we describe the divided echo subtraction (dES) sequence that is used to image musculoskeletal tissues with a very short  $T_2^*$ . These tissues include fascia, tendons, and aponeuroses. In this manuscript, we explain how this contrast is generated, review how these techniques are used in our research, and discuss the current challenges and limitations of this technique.

**Keywords:** MRI; contrast; traumatic brain injury; white matter; ultrashort- $T_2^*$ ; fascia; multiple sclerosis



**Citation:** Cornfeld, D.; Condron, P.; Newburn, G.; McGeown, J.; Scadeng, M.; Bydder, M.; Griffin, M.; Handsfield, G.; Perera, M.R.; Melzer, T.; et al. Ultra-High Contrast MRI: Using Divided Subtracted Inversion Recovery (dSIR) and Divided Echo Subtraction (dES) Sequences to Study the Brain and Musculoskeletal System. *Bioengineering* **2024**, *11*, 441. <https://doi.org/10.3390/bioengineering11050441>

Academic Editor: Andrea Cataldo

Received: 1 April 2024

Revised: 26 April 2024

Accepted: 28 April 2024

Published: 29 April 2024



**Copyright:** © 2024 by the authors. Licensee MDPI, Basel, Switzerland. This article is an open access article distributed under the terms and conditions of the Creative Commons Attribution (CC BY) license (<https://creativecommons.org/licenses/by/4.0/>).

## 1. Introduction: Soft Tissue Contrast

Soft tissue contrast is what differentiates different parts of the anatomy, and more importantly, normal from abnormal anatomy, on a medical image. The historic advantage of Magnetic Resonance Imaging (MRI) is that it provides superior soft tissue contrast compared to radiography, computed tomography, and ultrasound. The brightness, or signal, of a particular tissue on an MR image is based on specific properties of that tissue, combined with the particulars of the pulse sequence used for image acquisition. Contrast is the difference in signal between two tissues and/or fluids seen on an image.

Common tissue properties used for generating MR images include mobile proton density ( $\rho_m$ ), longitudinal relaxation ( $T_1$ ), and transverse relaxation ( $T_2$ ). These were first described by Felix Bloch in 1946 [1] but not in the context of medical imaging. Different tissues, by virtue of their different intra- and extra-cellular characteristics, have different tissue properties. Most clinical MR techniques are based on exploiting differences in tissue  $\rho_m$ ,  $T_1$ , and  $T_2$ . These include spin echo (SE), gradient echo, and inversion recovery (IR).

Other tissue properties include mean diffusivity ( $D^*$ ), susceptibility, perfusion, vascular permeability, chemical shift, and velocity. More advanced MRI techniques take advantage of these properties to generate contrast. For example, diffusion-weighted imaging (DWI), contrast-enhanced imaging, and phase-contrast imaging generate contrast based on differences in  $D^*$ , perfusion/vascular permeability, and velocity, respectively.

Some images are useful in their ability to distinguish different types of anatomy. Examples include the need to distinguish intracranial hemorrhage from normal gray and white matter, colon cancer metastases from the normal surrounding liver, and fluid from the ends of a torn and retracted muscle or tendon. In these examples, the pathology manifests as tissues with fundamentally different tissue properties. The  $\rho_m$ ,  $T_1$ , and  $T_2$  of blood are sufficiently different from those of gray or white matter to differentiate these tissues on an anatomic image. Colon cancer metastases have a sufficiently different  $\rho_m$ ,  $T_1$ ,  $T_2$ , and vascular permeability to liver to differentiate them from normal liver. Fluid and hemorrhage have a sufficiently different  $\rho_m$ ,  $T_1$ , and  $T_2$  from those of muscle and tendon to visualize them on MR images.

Some types of images are particularly valuable because of their ability to produce useful contrast from small changes in tissue properties from normal. Examples include diagnosing primary neoplasms and inflammation. Metastatic disease is relatively straightforward to diagnose, because the cancerous tissue is usually fundamentally different from the tissue it has metastasized into. However, primary neoplasms often have similar tissue properties to the organs they arise in. It is therefore difficult to identify hepatocellular carcinoma in the liver based only on  $\rho_m$ ,  $T_1$ , and  $T_2$ . For this reason, intravenous Gadolinium-enhanced MRI is used to generate contrast within the liver, based on differences in perfusion and capillary permeability. Likewise, the  $\rho_m$ ,  $T_1$ , and  $T_2$  changes in gray and white due to acute stroke are also very small. Detection of acute stroke uses a technique that generates contrast based on changes in tissue  $D^*$ .

The earliest MRI pulse sequences (or image acquisition techniques) were often better than CT in identifying normal anatomy: SE and gradient echo pulse sequences take advantage of differences in  $\rho_m$ ,  $T_1$ , and  $T_2$  to provide excellent anatomic images of the brain, musculoskeletal system, and abdominal organs. Varying certain specifics of the image acquisition allows a sequence to be sensitive to differences in tissue  $\rho_m$ ,  $T_1$ , or  $T_2$ , leading to the concept of  $\rho_m$ -,  $T_1$ -, and  $T_2$ -weighted images, where the brightness of a tissue on an image is mostly attributable to a single tissue property.

The evolution of MRI since the mid 1980's has been to develop improved techniques for distinguishing normal anatomy from changes due to disease. Two examples include imaging in multiple sclerosis (MS) and imaging short  $T_2^*$  musculoskeletal tissues such as cortical bone, fascia, tendons, and aponeuroses.

### 1.1. Imaging of MS

In the early 1980s, IR techniques, which will be explained later in the manuscript, distinguished MS plaque from background white matter, based on the  $T_1$  differences between plaque and normal white matter [2]. Increased plaque  $T_1$  compared to white matter  $T_1$  resulted in an increased signal on the images. Subsequent SE techniques were able to identify plaque based on differences in  $T_2$  [3–6]. Increased plaque  $T_2$  compared to white matter  $T_2$  resulted in an increased signal on the images.

Because plaques were noted to result in both increased white matter  $T_1$  and  $T_2$ , the STIR sequence was developed in 1985 to generate increased contrast due to increases in both tissue  $T_1$  and  $T_2$  [7]. This improved sensitivity in detecting subtle plaques meant that white matter with smaller increases in  $T_1$  and  $T_2$  could be discerned from the normal background tissue. In 1992, the FLAIR sequence was developed to null bright signals from cerebrospinal fluid (CSF), making it easier to see changes near the extra-axial spaces [8]. This provided a visually appealing image, and FLAIR has become the standard-of-care clinical sequence for imaging cerebral white matter. However, with the FLAIR sequence, the effects of  $T_1$  and  $T_2$  on tissue brightness are opposed: increased tissue  $T_1$  results in a

decreased signal and increased tissue  $T_2$  results in an increased signal. STIR may therefore be more sensitive for detecting subtle plaque, because the  $T_1$  and  $T_2$  effects on the signal are synergistic.

Techniques such as DIR (double IR) [9] and MP2RAGE [10], developed in 1985 and 2010, respectively, take two IR sequences obtained with different parameters and multiply them together to create images sensitive to small changes in  $T_1$  and  $T_2$ . Both sequences have been shown to be superior for detecting focal MS plaques in the gray matter compared to the standard of care, FLAIR [11,12]. In 2019, the FLAWShc (Fluid and White matter Suppression, high contrast) sequence was described [13], in which two IR sequences with widely different inversion times are subtracted, then divided by their sum, similar to the divided Subtracted Inversion Recovery (dSIR) sequence described in this paper, but not using magnitude reconstruction or variable inversion times. FLAWShc sequences have been used to detect cortical lesions in MS [14]. DIR, MP2RAGE, and FLAWShc are noted for their high gray/white matter contrast.

Diffusion-weighted and intravenous Gadolinium-enhanced images have been used to image MS but have not proven to be more sensitive for detecting early changes in the disease. Rather, changes in plaque  $D^*$  and perfusion/vascular permeability are used as markers of active inflammation at previously known sites of disease [15].

Although the imaging findings for MS are focal, MS is a systemic disease of the white matter [16]. Focal MS plaques represent permanent damage to the white matter and do not regress with treatment. We have hypothesized that subtle, potentially reversible, pathologic changes in white matter are manifest on imaging as small changes in  $T_1$  that are too small to detect with currently used sequences. We also hypothesize that these more subtle diffuse changes (which we are calling neuroinflammation, without knowledge of its true etiology) exist in other generalized brain disorders, such as mild traumatic brain injury (mTBI), substance abuse, and post-viral syndromes such as long COVID.

With this in mind, the subtracted inversion recovery (SIR) image was described in 2017 and 2018 as a pixel-by-pixel subtraction of two IR sequences, resulting in an image with an increased sensitivity to small changes in  $T_1$  but only between two specific values of  $T_1$  [17,18]. The range of  $T_1$ s where the sequence is highly sensitive to changes is called the middle domain (mD) of the sequence. This allows for targeted imaging of the white matter that is twice as sensitive to small changes in white matter  $T_1$  than current clinical sequences.

In 2022 and 2023 we described the dSIR technique, which is even more sensitive to small changes in  $T_1$  [19,20]. This sequence takes two images obtained using the IR technique and generates a third image by performing a voxel-by-voxel division of their difference by their sum. This is called “divided subtraction”. As we will demonstrate, dSIR images show high sensitivity in imaging small changes in white matter  $T_1$  from normal.

### 1.2. Soft Tissue Contrast in MSK

Soft tissue contrast in musculoskeletal (MSK) imaging presents unique challenges. Tissues with short (1–10 ms) and ultrashort (0.1–1 ms)  $T_2^*$ s are difficult to image, but a wide range of techniques have been developed to do this. The relevant tissues include cortical bone, myelin, fascia, aponeuroses, and lung. The  $T_2^*$  tissue property is similar to the  $T_2$  tissue property and, in the context of short TE imaging, will be used interchangeably. As we will show later, the signal from these tissues quickly drops to zero after excitation, making them difficult to image directly without specialized techniques.

Advances in gradient hardware and radiofrequency (rf) switching have facilitated the development of ultrashort TE (UTE) and zero TE (zTE) sequences that can capture signals from short and ultrashort  $T_2^*$  tissues. Longer  $T_2$  soft tissues (such as white matter, gray matter, fat, abdominal soft tissues, muscle, blood, and fluid) also appear bright on these images, providing that repetition times (TR—to be discussed subsequently) are chosen to allow full recovery of their longitudinal magnetizations.

Imaging with zTE captures the signal from cortical bone and fascia, which still remain low-signal compared to other tissues due to their low mobile proton densities [21,22].

Long  $T_2^*$  tissues are high-signal on these images but show little contrast between them. Following bias correction and intensity normalization, these images can be displayed with an inverted gray scale, so that the cortical bone and fascia appear high-signal (bright) and long  $T_2^*$  tissues appear low-signal (dark). Most currently available commercial MR scanners include this option for imaging cortical bone (Figure 1).

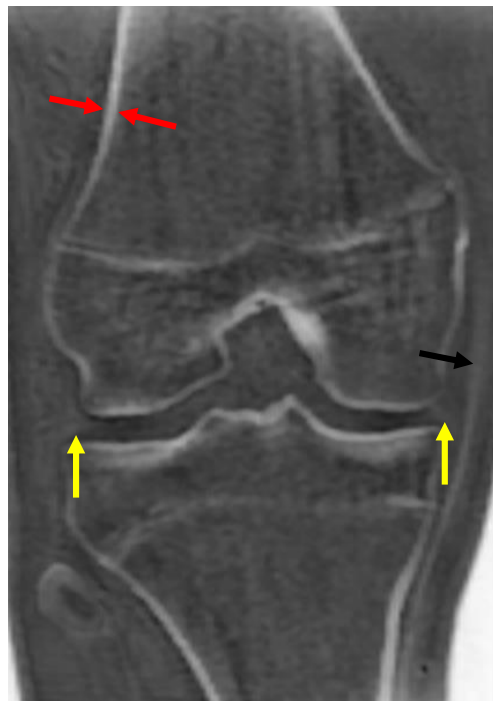


**Figure 1.** Coronal zTE image of the knee displayed with an inverted gray scale. Cortical bone (red arrow) is bright. Other short  $T_2$  tissues, such as the medial collateral ligament (black arrow) and the menisci (yellow arrows), are also bright, but less so than the cortical bone.

An echo subtraction (ES) technique has been described, in which images obtained using a short TE are subtracted from images obtained with an ultrashort TE. The workings of this sequence are explained subsequently. ES is used to suppress signals from long  $T_2^*$  tissue components. In 2018, the 3D DIR-UTE-cones sequence was described [23], which uses an ultrashort TE to detect signals from ultrashort  $T_2^*$  tissues and suppresses signals from longer- $T_2^*$  water- and fat-containing tissues by using adiabatic inversion pulses to null their longitudinal magnetizations.

In 2022, we introduced the divided echo subtraction (dES) sequence [24]. The dES sequence obtains two images with ultrashort and short echo times and performs a voxel-by-voxel subtraction, followed by division by the sum of the two images. ES produces a band-pass  $T_2^*$  filter with a low signal in the lower ultrashort  $T_2^*$  domain, and dES produces a low-pass  $T_2^*$  filter with a high signal in the lower ultrashort  $T_2^*$  domain. This is important for producing a high signal from cortical bone and other tissues such as myelin with significant low ultrashort  $T_2^*$  components.

## 2. Divided Subtraction MRI

The divided subtraction technique can be generalized as a simple mathematical manipulation of otherwise basic MRI pulse sequences, as will be explained subsequently. We have applied it to  $T_1$ -weighted images for the targeted evaluation of white matter and separately to ultrashort  $T_2$ -weighted images for the evaluation of bone and fascia. The  $T_1$  technique is called dSIR. The  $T_2$  technique is called dES.

Division and subtraction is a novel way of generating increased MR contrast from otherwise basic and readily available pulse sequences. The image processing is fast and

comprised of simple image arithmetic. In addition to imaging white matter, dSIR can also produce images targeted to specific tissues and small changes in the  $T_1$  of these tissues due to disease. The technique can easily be optimized for different diseases in different parts of the body. We call this approach targeted MRI (tMRI). For  $T_2$ -weighted images, dES is used to create images of cortical bone, fascia, aponeuroses, and tendons.

This review introduces the divided subtracted technique, as implemented for  $T_1$ - and  $T_2$ -weighted images in the brain and musculoskeletal systems, respectively. We introduce the tissue property filter paradigm to explain how this contrast is generated. This paradigm simplifies the workings of many MR imaging techniques but is rarely used in the literature. We describe how we implemented divided subtraction sequences in our research and provide specific examples. We also discuss the current challenges and limitations of this technique, including comparisons with similar methods. Lastly, we provide examples of other potential applications.

### 3. Tissue Contrast in MRI and Theory behind dSIR and dES

When placed into a strong, static magnetic field ( $B_0$ ), the magnetic moments of a patient’s water protons align to form a net magnetization ( $M_0$ ) parallel to the  $B_0$ . The  $M_0$  can be rotated by applying a radiofrequency (rf) pulse at the Larmour frequency for hydrogen at the field strength of the  $B_0$ . Once rotated, the net magnetic moment precesses about the axis of the  $B_0$  and can be represented in the rotating frame by two components: a longitudinal magnetization ( $M_z$ ) parallel to the axis of the  $B_0$  and a transverse magnetization ( $M_{xy}$ ) perpendicular to the  $B_0$ .

The following Bloch equations describe the behavior of  $M_z$  and  $M_{xy}$  immediately after the  $M_0$  is rotated  $90^\circ$ , with the flip being instantaneous and occurring at  $t = 0$ .  $T_1$  and  $T_2$  are tissue properties specific to the tissue being imaged.

$$M_z(t) = M_0 \left(1 - e^{-t/T_1}\right) \tag{1}$$

$$M_{xy}(t) = M_0 e^{-t/T_2} \tag{2}$$

At time  $t$ , a detector measures the magnitude of  $M_{xz}$ , which is referred to as signal  $S$ . An MR pulse sequence is a set of machine instructions to apply an rf pulse to the tissue magnetization, wait a predefined period, then measure this signal. This process is repeated multiple times. By varying the time between repetitive rf pulses (called TR) and the time between the rf pulse signal detection (called TE), the measured signal varies based on tissue  $\rho_m$ ,  $T_1$ ,  $T_2$ , or some combination of all three. The TR and TE are referred to as the pulse sequence parameters and are under the control of the operator.

#### 3.1. Spin Echo

Traditional SE pulse sequences use a flip angle ( $\alpha$ ) of  $90^\circ$  and a TR sufficiently long such that  $M_{xy} = 0$  when  $t$  in Equation (2) equals TR. The signal  $S$  emanating from a specific tissue as measured by the detector is

$$= K \rho_m \times \left(1 - e^{-TR/T_1}\right) \times e^{-TE/T_2} \tag{3}$$

where  $K$  is a scaling function. A more explicit rendering of Equation (3) in terms of tissue properties is as follows:

$$S = S_{\rho_m}(\rho_m) \times S_{T_1}(T_1) \times S_{T_2}(T_2) \tag{4}$$

$$S_{PD}(\rho_m) = \rho_m \tag{5}$$

$$S_{T_1}(T_1) = \left(1 - e^{-TR/T_1}\right) \tag{6}$$

$$S_{T_2}(T_2) = e^{-TE/T_2} \tag{7}$$

It should be noted that the fast spin echo (FSE) technique is almost uniformly used instead of the SE technique. Equations (3)–(7) are also valid for the FSE technique, with the caveat that the parameter TE actually refers to an “effective” TE. The specific differences between SE and FSE are beyond the scope of this manuscript, and the terms are used here interchangeably.

Equations (4)–(7) recast Equation (3) into three independent components each dependent on a tissue property that is explicitly identified as the dependent variable and a sequence parameter that is explicitly identified as a constant parameter of the sequence. We call Equations (5)–(7) tissue property filters: one for  $\rho_m$ , one for  $T_1$ , and one for  $T_2$ . They allow for a mathematical explanation of how changes in tissue property affect the signal. This paradigm was first described by Bydder and Young in 2020 [25].

Figure 2 shows the  $\rho_m$ ,  $T_1$ , and  $T_2$  tissue property filters for the SE sequence with  $\alpha = 90^\circ$ , TR = 700 ms, and TE = 5 ms. Each plot shows the contribution of a tissue property to differences in signal, or contrast, between tissues. Most soft tissues have the same  $\rho_m$ , and therefore  $\rho_m$  does not generate contrast. Most soft tissues are distributed along the steep part of the  $S_{T_1}(T_1)$  curve, such that their different  $T_1$  properties result in contrast (i.e., a different signal). While some tissues have similar  $T_1$  values (white matter and liver, for example), these are in different parts of the body and are not typically imaged at the same time. Most tissues are distributed along the flat part of the  $S_{T_2}(T_2)$  curve, such that their different  $T_2$  properties do not result in contrast. Muscle and tendons are an exception. This is therefore called a “ $T_1$ -weighted” sequence, because *most* of the contrast between tissues is due to their different  $T_1$  values. In practice, all sequences produce a mixed contrast, and the relative amount of contrast due to each tissue property can be derived mathematically; however, this is beyond the scope of this discussion.

Figure 3 shows the  $\rho_m$ ,  $T_1$ , and  $T_2$  tissue property filters for the SE sequence with  $\alpha = 90^\circ$ , TR = 5000 ms, and TE = 100 ms. Most soft tissues have the same  $\rho_m$ , and therefore  $\rho_m$  does not generate contrast. Most soft tissues are distributed along the flat part of the  $S_{T_1}(T_1)$  curve, such that their  $T_1$  properties result in a similar signal. Most tissues are distributed along the steep part of the  $S_{T_2}(T_2)$  curve, such that their differences in  $T_2$  result in contrast. This is therefore called a “ $T_2$ -weighted” sequence because *most* of the contrast between tissues is due to their different  $T_2$  values.

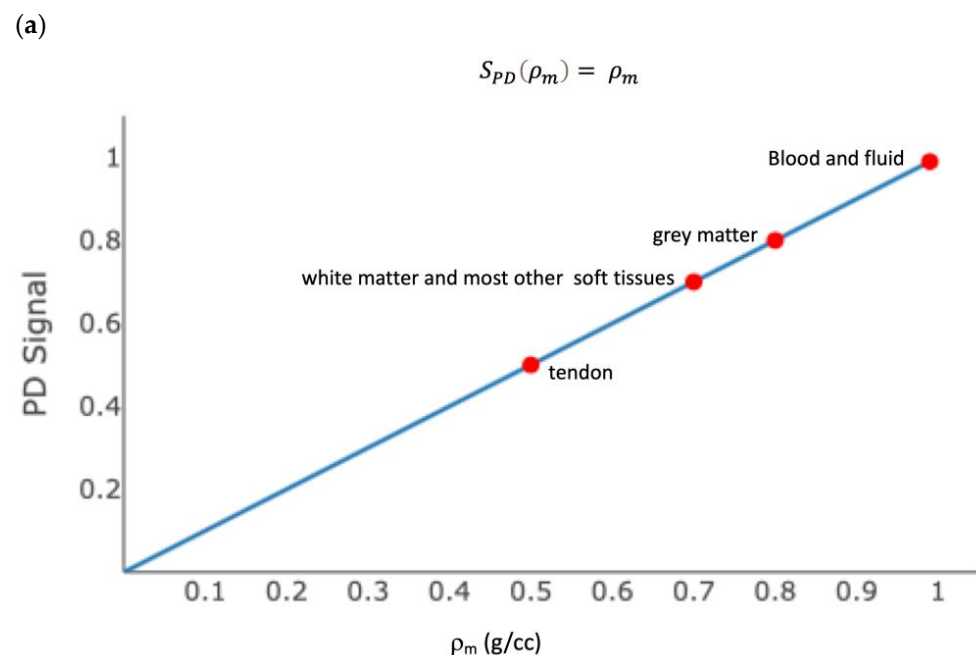
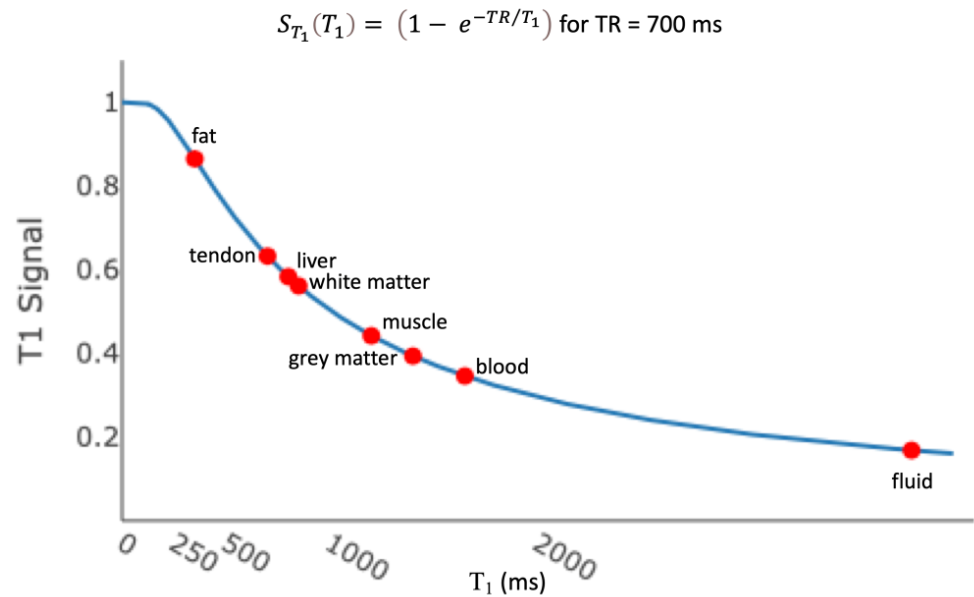
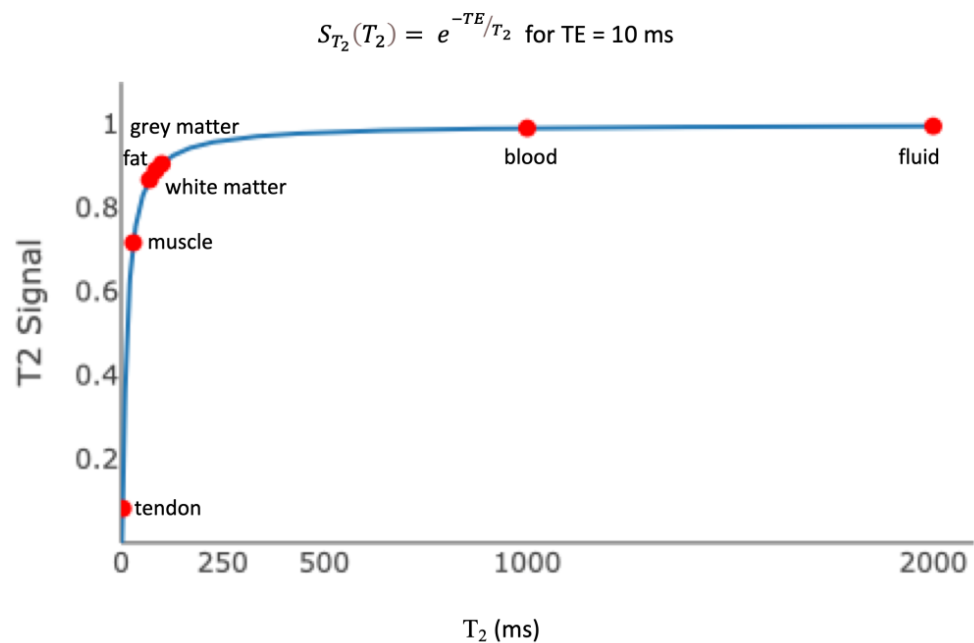


Figure 2. Cont.

(b)



(c)

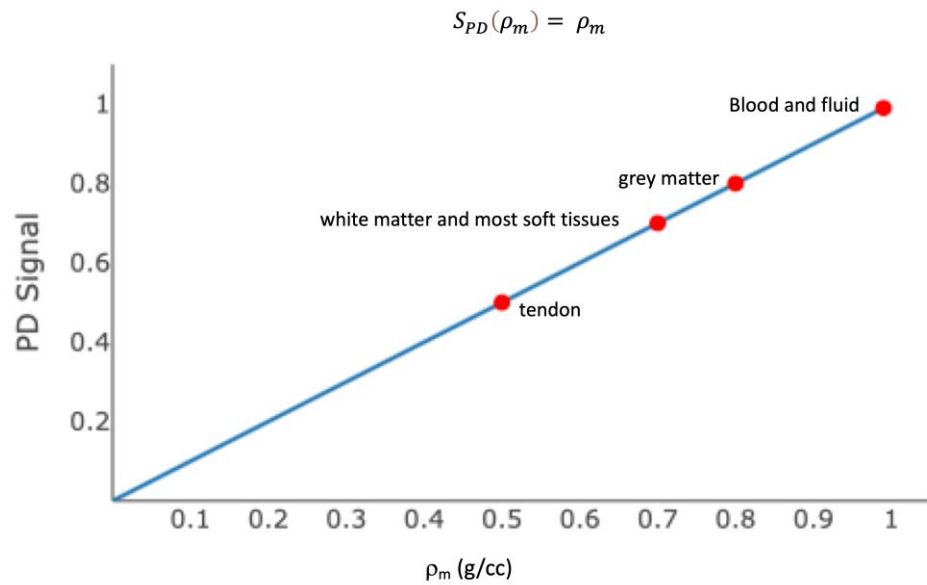


**Figure 2.** Tissue property filters for a  $T_1$ -weighted image. (a) The proton density ( $\rho_m$ ) filter for the fast spin echo sequence shows the signal due to  $r_m$  in an image. (b) The  $T_1$  filter for the fast spin echo sequence, with TR = 700 ms, shows the signal due to  $T_1$  in an image. Most tissues sit on the steep part of the curve, which results in different signals from different tissues based on  $T_1$  weighting. (c) The  $T_2$  filter for the fast spin echo sequence, with TE = 10 ms, shows the signal due to  $T_2$  in an image. Most tissues sit on the flat part of the curve, which results in little contrast between tissues based on  $T_2$  weighting. Muscle and tendon are the exception. Changes in tendon  $T_2$  are easily visualized on fast spin echo sequences, with TE = 10 ms, because the curve is steep at the  $T_2$  of tendon.

$T_1$ - and  $T_2$ -“weighted” SE and FSE sequences are generally good for distinguishing anatomy. However, as discussed previously, the detection of subtle disease requires small

changes in a tissue property to result in large changes in signal. The sensitivity of a sequence for detecting these small changes within a tissue is the slope of the filter at the  $T_1$  or  $T_2$  value of the tissue. The slope, by definition, is the change in signal for a given change in tissue property. If the slope is positive, an increase in tissue property results in an increased signal. If the slope is negative, an increase in tissue property results in a decreased signal. For small changes in white matter  $T_1$  to result in a noticeable change in signal, the  $T_1$  of white matter must sit on a steep part of the  $S_{T_1}(T_1)$  curve. The slope of Equation (6), with  $TR = 700$  (Figure 2b) at the  $T_1$  of white matter (850 ms in a 3 Tesla scanner), is  $-4.3 \times 10^{-4}/\text{ms}$  (arbitrary signal units on the y-axis per ms on the x-axis). A typical “ $T_1$  weighed” FSE image of the brain is shown in Figure 4. Gray matter is darker than white matter, and fluid is darker than gray matter.

(a)



(b)

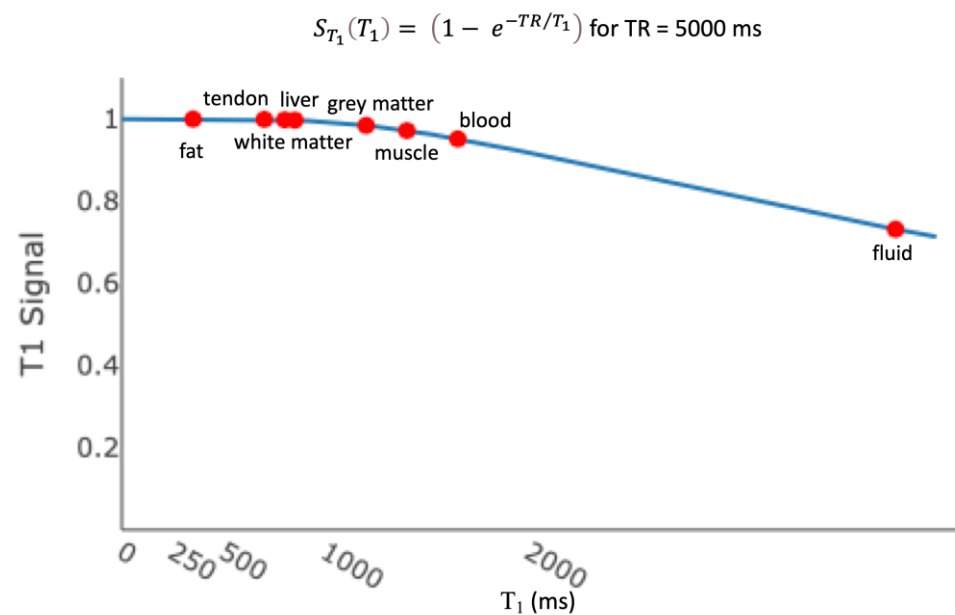
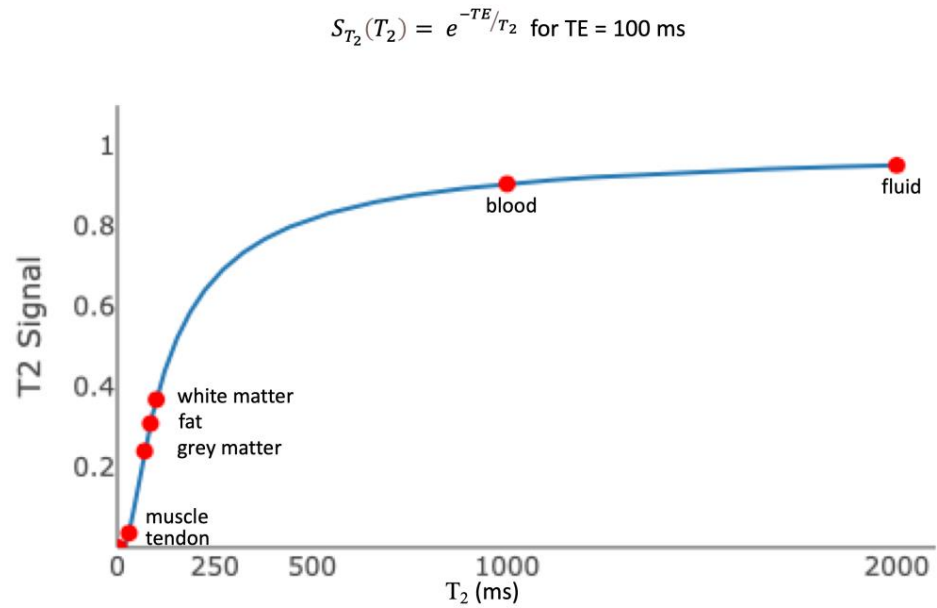
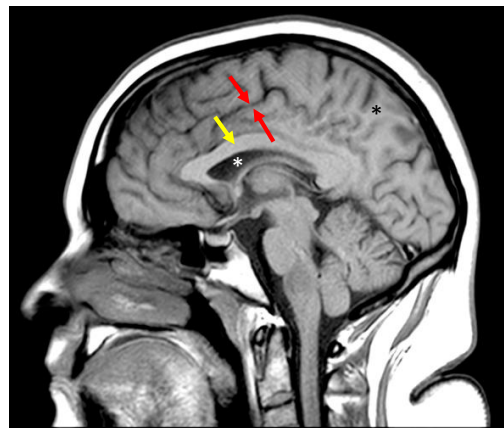


Figure 3. Cont.

(c)



**Figure 3.** Tissue property filters for a T<sub>2</sub>-weighted image. (a) The proton density ( $\rho_m$ ) filter for the fast spin echo sequence shows the signal due to  $r_m$  in an image. (b) The T<sub>1</sub> filter for the fast spin echo sequence, with TR = 5000 ms, shows the signal due to T<sub>1</sub> in an image. Most tissues sit on the flat part of the curve, which results in little signal difference between different tissues. (c) The T<sub>2</sub> filter for the fast spin echo sequence, with TE = 100 ms, shows the signal due to T<sub>2</sub> in an image. Most tissues sit on the steep part of the curve, which results in a contrast between tissues based on T<sub>2</sub> weighting.



**Figure 4.** Sagittal fast spin echo image of the brain with TR = 700 ms and TE = 10 ms. Gray matter (between the red arrows) is darker than the subcortical white matter (black asterisk) and corpus callosum (yellow arrow). Fluid (white asterisk) is even darker. This parallels the curve in Figure 2b.

### 3.2. Inversion Recovery

An IR sequence uses a series of sequential 180° and 90° flips. The time between two 180° flips is called TR. The time between the 180° flip and 90° flip is called TI. The detector is turned on at a time TE, following the 90° flip. The equation that describes the behavior of M<sub>Z</sub>, and hence the signal due to T<sub>1</sub> immediately after a 90° flip, is

$$S(T_1) = \left| 1 - 2e^{-\frac{TI}{T_1}} + e^{-\frac{TR}{T_1}} \right|. \tag{8}$$

and it is plotted in Figure 5a.

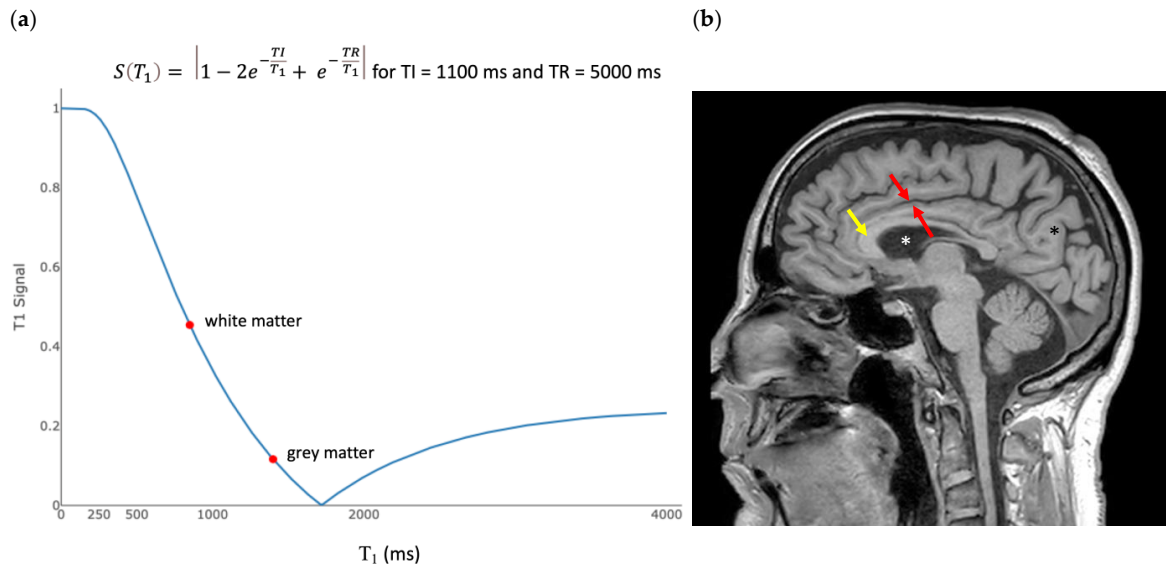


**Figure 5.** Inversion recovery  $T_1$  filter. (a)  $T_1$  tissue property filter for the IR sequence with  $TI = 1100$  ms and  $TR = 5000$  ms. Tissues with  $T_1 = 1594$  ms are nulled by these parameters. The slope of the curve in the region of most tissues of interest is negative, so that an increase in  $T_1$  results in a decreased signal. This produces an image like an SE  $T_1$ -weighted image. The slope of the left half of the filter is steeper than the slope of the plot in Figure 2b, resulting in increased contrast. (b) Sagittal fast spin echo image of the brain with  $TR = 5000$  ms and  $TE = 1000$  ms. Gray matter (between the red arrows) is darker than the subcortical white matter (black asterisk) and corpus callosum (yellow arrow). Fluid (white asterisk) is even darker. This parallels the curve in (a). There is increased contrast compared to Figure 4, which reflects the larger difference in signal between gray and white matter in (a) than in Figure 2b.

The slope of Equation (8), with  $TR = 5000$  ms and  $TI = 1000$  ms at the  $T_1$  of white matter, is  $-8.2 \times 10^{-4}/\text{ms}$ . The sensitivity of the IR sequence to small changes in the  $T_1$  of white matter is therefore nearly twice that of the “ $T_1$ -weighted” SE sequence (Table 1). A typical “ $T_1$ -weighted” FSE-IR image of the brain is shown in Figure 5b.

**Table 1.** Maximum slopes of the  $T_1$  tissue property filters.

Sequence	Relevant Parameters	Slope of the $T_1$ Filter at the $T_1$ of White Matter	Ratio of the Maximum Slope to the FSE Sequence
FSE	$TR = 700$ ms	$-4.3 \times 10^{-4}/\text{ms}$	1
FSE-IR	$TR = 5000$ ms, $TI = 1000$	$8.2 \times 10^{-4}/\text{ms}$	1.9
SIR	$TR = 5000$ ms, $TI_{\text{short}} = 580$ , $TI_{\text{long}} = 970$	$16 \times 10^{-4}/\text{ms}$	3.7
dSIR wide mD	$TR = 5000$ ms, $TI_{\text{short}} = 580$ , $TI_{\text{long}} = 970$	$43 \times 10^{-4}/\text{ms}$	10
dSIR narrow mD	$TR = 5000$ ms, $TI_{\text{short}} = 580$ , $TI_{\text{long}} = 740$ ms	$87 \times 10^{-4}/\text{ms}$	20.2

FSE—fast spin echo; FSE-IR—fast spin echo inversion recovery; SIR—subtracted inversion recovery; sDIR—divided Subtracted Inversion Recovery; mD—middle domain; TR—repetition time; TE—echo time;  $TI_{\text{short}}$ —shorter inversion time;  $TI_{\text{long}}$ —longer inversion time.

A specific feature of the IR sequence is that the signal is nulled for tissues with a specific  $T_1$ . The  $T_1$  resulting in zero signal is determined by the choice of  $TI$ , or time between the  $180^\circ$  and  $90^\circ$  rf pulses. For a sufficiently long  $TR$ , the  $T_1$  that is nulled can be calculated by setting Equation (8) to zero and solving for  $T_1$ . This results in  $T_{1\text{nulled}} = 1.45 \times TI$ .

### 3.3. Subtracted Inversion Recovery

Figure 6a shows the plot of two IR  $T_1$  tissue filters. The red curve is a plot of Equation (8), with  $TI = 580$  ms (call this  $TI_{short}$ ) and  $TR = 5000$  ms, and results in tissues with the  $T_1$  values of white matter being nulled. This results in an unusual image, where white matter is black and gray matter is bright (Figure 6b). Increases in white matter  $T_1$  from normal result in an increased signal, which is the opposite of what is expected from a standard  $T_1$ -weighted sequence.

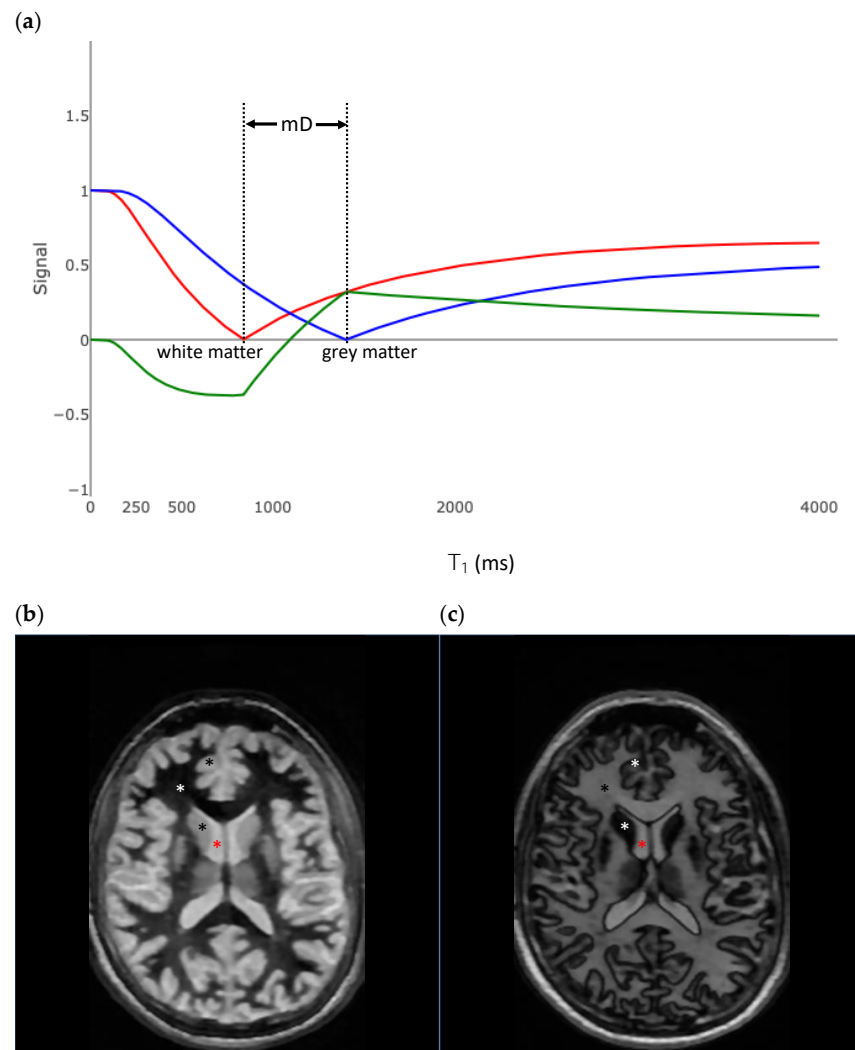


**Figure 6.** Subtracted inversion recovery (SIR) sequence. (a)  $T_1$  tissue property filter for the SIR sequence. The red curve uses a  $TI_{short}$  designed to null white matter. The blue curve uses a  $TI_{long}$  designed to null gray matter. The middle domain (mD) is the range of  $T_1$ s between the tissues nulled by  $TI_{short}$  and  $TI_{long}$ . The green curve is the tissue filter for the SIR sequence and is the blue curve subtracted from the red curve. The slope of the green curve at the  $T_1$  of white matter is nearly two times the maximum slope of the red or blue curves. (b) Axial fast spin echo inversion recovery image, with  $TR = 5000$  ms and  $TI = 580$  ms, designed to null white matter. The slope of the  $T_1$  filter to the right of white matter (red curve in (a)) is reversed compared to the filters in 5a and 2b. Increases in  $T_1$  result in increased signal, and gray matter (black asterisk) is brighter than white matter (white asterisk). Fluid (red asterisk) is brighter than gray matter. (c) Axial fast spin echo inversion recovery image, with  $TR = 5000$  ms and  $TI = 970$  ms, designed to null gray matter. The slope of the  $T_1$  filter to the right of the white matter (blue curve in (a)) is the same compared to the filters in Figures 5a and 2b. Increases in  $T_1$  result in decreased signal, and gray matter (black asterisk) is darker than white matter (white asterisk). Fluid (red asterisk) is brighter than gray matter.

The blue curve in Figure 6a is a plot of Equation (8), with  $TI = 970$  ms (call this  $TI_{high}$ ) and  $TE = 5000$  ms, and results in tissues with the  $T_1$  values of gray matter being nulled. This results in an image like that produced by the IR  $T_1$  in Figure 5a, only the gray matter appears black.

The green curve in Figure 6a is the  $T_1$  filter for the SIR image and is the result of subtracting the blue curve from the red curve in the central region. Visually, the slope of the green curve is steeper than either the red or blue curves. The slope of the green curve at the  $T_1$  of the white matter (850 ms) is  $16 \times 10^{-4}/ms$ , which is steeper than each of the individual  $T_1$  filters. On an SIR image, normal white matter is black, and small increases in white matter  $T_1$  result in an increased signal (Figure 7) This increased sensitivity for small changes in  $T_1$  is only applicable in the middle domain (mD), between the  $T_1$  values of white and gray matter. If  $TI_{high}$  is decreased, then the mD narrows, and the slope in the mD (and as a result, the contrast generated from a change in  $T_1$ ) is increased. Conversely, as the mD is widened, the contrast decreases.



**Figure 7.** Sagittal subtracted inversion recovery (SIR) images in a patient with multiple sclerosis (MS). (a) Sagittal SIR image in an asymptomatic patient with MS presenting for a routine follow-up using a wide mD.  $TR = 5000$ .  $TI_{short} = 450$  to null white matter.  $TI_{long} = 850$  to null gray matter. This is considered a wide mD image. The normal white matter is black. A “Dawson’s finger” (red arrow) is seen as an increased signal. Small plaques (white arrows) are also identified as areas of increased signal. The increased signal is due to increased  $T_1$  in the abnormal white matter. The contrast on the image is described by the green curve in Figure 6a. (b) Sagittal T<sub>2</sub>-FLAIR image in the same patient

as in (a). The “Dawson’s finger” and small plaques are also seen as areas of increased signal, only the signal is due to increases in white matter  $T_2$ . All the plaques seen on the SIR were also seen on the  $T_2$ -FLAIR. (c) Sagittal inversion recovery fast spin echo  $T_1$  image in the same patient as in (a,b). The Dawson’s finger and small plaques are dark compared to normal white matter, as per the curve shown in Figure 5a. This contrast is due to increases in white matter  $T_1$ . Compare the contrast between normal and abnormal white matter with the image in (a). The abnormal white matter is more conspicuous in (a). This is because the maximum slope of the SIR filter (the green curve in Figure 6a) is nearly twice that of the IR filter (red and blue curves in Figure 6a and blue curve in Figure 5a). See Table 1.

### 3.4. Subtracted Division Inversion Recovery

The red and blue plots in Figure 8a are the same IR  $T_1$  tissue filters shown in Figure 6a. The purple plot is the  $T_1$  filter for the divided Subtracted Inversion Recovery (dSIR) image. This  $T_1$  filter is the difference of the blue and red graphs divided by their sum. The slope of this filter at the  $T_1$  of white matter is  $43 \times 10^{-4}/\text{ms}$ . This is 2.6 times the slope of the SIR sequence, 5.4 times the slope of the IR sequence, and 10 times the slope of the SE sequence (Table 1). This increased sensitivity is only applicable for tissues with  $T_1$  values in the mD between the  $T_1$ s nulled by the two IR acquisitions. As the mD narrows, the slope steepens. Figure 8b shows the bipolar dSIR  $T_1$  filter, where the blue plot is derived from Equation (8) with a  $TI_{\text{high}}$  of 750 ms. Compared to Figure 8a, the mD of the sDIR  $T_1$  filter is narrower and the slope within the mD is greater. The slope of this filter at the  $T_1$  of white matter is  $87 \times 10^{-4}/\text{ms}$ , which is twenty times the slope of the SE filter in Figure 2b (Table 1). Normal white matter appears black on this image. Very small increases in white matter  $T_1$  from normal appear bright.

Modifying  $TI_{\text{high}}$  and  $TI_{\text{short}}$  controls two aspects of the image. First,  $TI_{\text{long}}$  and  $TI_{\text{short}}$  determine what tissues are best imaged. Figure 8a,b show a dSIR filter targeted to detect small changes in white matter. Figure 8c shows a dSIR filter targeted to detect small changes in the  $T_1$  of gray matter. The red curve is Equation (8), with  $TI_{\text{short}} = 970$  ms designed to null signal from gray matter. The blue curve is Equation (8), with  $TI_{\text{long}} = 1200$  ms which was chosen to be higher than 970 ms.  $TI_{\text{long}}$  and  $TI_{\text{short}}$  can be chosen to target  $T_1$  changes within any range of tissues. Second, as  $\Delta TI$  ( $TI_{\text{long}} - TI_{\text{short}}$ ) decreases, the slope of the filter in the mD, and thus the sensitivity to small changes in  $T_1$ , increases.

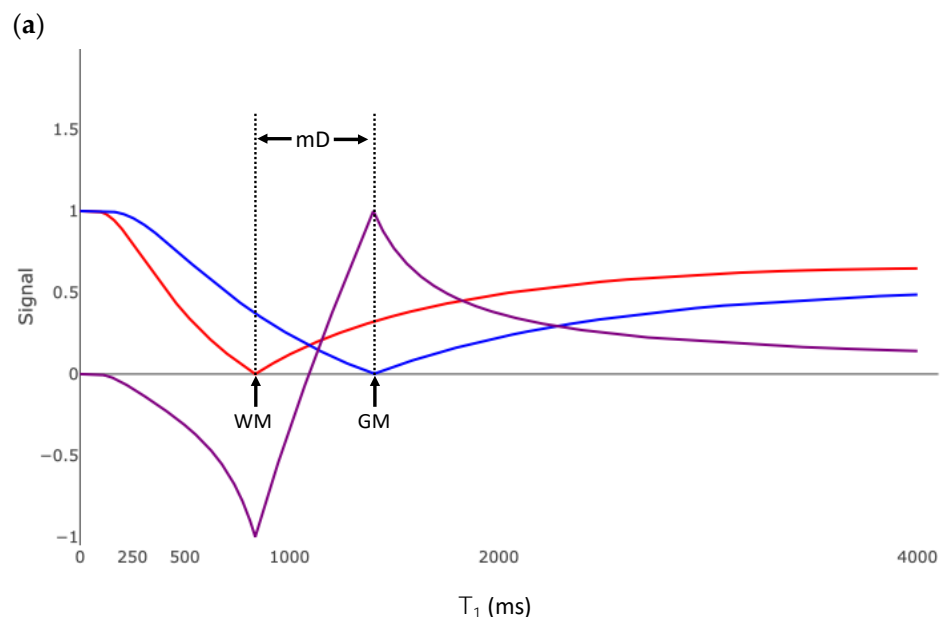
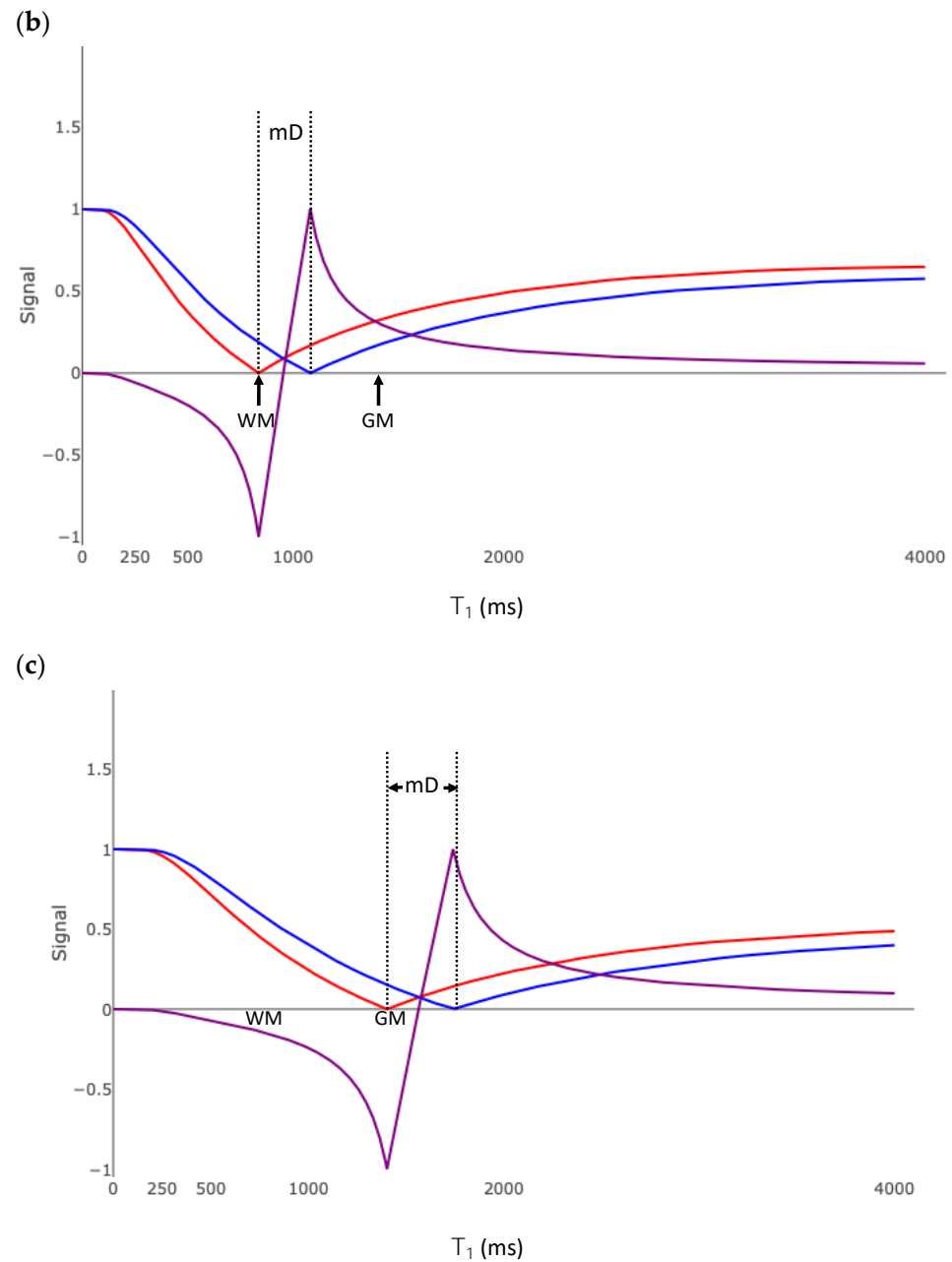


Figure 8. Cont.



**Figure 8.** Divided Subtracted Inversion Recovery (dSIR) T<sub>1</sub> filter. (a) The red curve is an inversion recovery (IR) sequence, with T<sub>1short</sub> chosen to null white matter. The blue curve is the filter for an IR sequence, with T<sub>1long</sub> chosen to null gray matter. The purple curve is the dSIR filter and is the division of the difference of the blue and red curves by their sum. The slope of the purple curve is 2.7 times the maximum slope of the curve in Figure 5a (which is the same as the maximum slope of the red and blue curves). The middle domain is the range of T<sub>1</sub> values between the tissues nulled by T<sub>1short</sub> and T<sub>1long</sub>, which in this case are white and gray matter. (WM—white matter; GM—gray matter; mD—middle domain). (b) T<sub>1</sub> filter for the dSIR sequence with a narrow middle domain compared to the curve shown in (a). As the middle domain decreases, the slope of the purple curve increases. (c) T<sub>1</sub> filter for a dSIR sequence targeted for changes in the T<sub>1</sub> of gray matter. T<sub>1short</sub> is chosen to null signal from gray matter. T<sub>1long</sub> is chosen to be higher. The width of the middle domain determines the sensitivity of the sequence to small changes in T<sub>1</sub>. “WM” marks the T<sub>1</sub> of white matter. “GM” marks the T<sub>1</sub> of gray matter.

When dSIR is targeted to white matter, the normal white matter is predominantly dark (Figure 9). When using a wide mD with T<sub>1long</sub> targeted to null gray matter, the gray matter

is bright. Using a narrow mD with  $TI_{long}$  targeted to null tissues with a  $T_1$  value between those of gray and white matter, the gray matter is an intermediate signal, and there is a high signal boundary between the white and gray matter and between white matter and CSF. The high signal boundaries can be explained mathematically [19] but are summarized as follows. Voxels located in the transition region at the boundary between two tissues contain mixtures of the two tissues and have  $T_1$  values between those of voxels which contain only one of the two tissues. If the  $T_1$  filter has a maximum value at a  $T_1$  between the  $T_1$  s of the pure tissues, the boundary will be high-signal. If the  $T_1$  filter has a minimum value between these two  $T_1$  values, the boundary will be low-signal. The literature describes at least 10 different types of white matter, each having different  $T_1$  values. These can be discerned on narrow mD dSIR images. The white matter is not homogeneously dark.

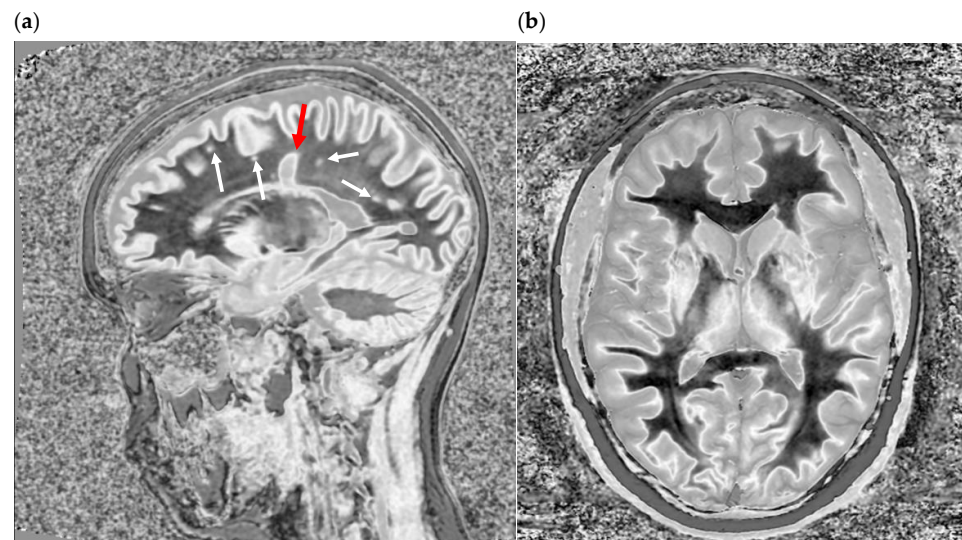


**Figure 9.** Divided Subtracted Inversion Recovery (dSIR) images. (a) Sagittal dSIR image of the same slice and patient as in Figure 7a–c.  $TR = 5000$  ms.  $TI_{short} = 450$  to null white matter.  $TI_{long} = 850$  to null gray matter.  $TE = 7$  ms. This is considered a wide mD image. The normal white matter is black. A “Dawson’s finger” (red arrow) is seen as an increased signal. Small plaques (white arrows) are also identified as areas of increased signal. The increased signal is due to increased  $T_1$  in the abnormal white matter. The contrast on the image is described by the purple curve in Figure 8a. The contrast between the normal and abnormal white matter is 2.7 times that of the SIR image in Figure 5 and 5 times that of the IR image in Figure 7c. (b) Axial narrow mD dSIR in a healthy volunteer.  $TR = 5000$ .  $TI_{short} = 350$ .  $TI_{long} = 500$ .  $TE = 7$  ms,  $TR = 5000$  ms. The normal white matter is black. Normal gray matter is intermediate signal. There is a high signal boundary between the gray and white matter, because the tissue filter (purple graph in Figure 8b) has a maximum between the  $T_1$  values of white matter and gray matter. Note that the gray matter is not as bright as on the wide mD dSIR image, as in (a). Compare the y-axis values (signal) of the purple curves in Figure 8a,b at the  $T_1$  of gray matter.

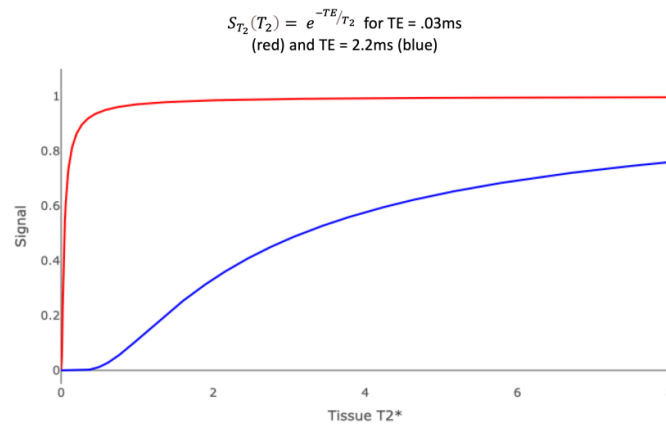
In summary, dividing the difference of two IR sequences (identical except for different inversion times) by their sum results in a sequence that is very heavily and almost purely  $T_1$  weighted for tissues with  $T_1$  values between those of the tissues nulled by the two inversion times. This is accomplished by acquiring two IR images, then performing a pixel-wise addition, subtraction, and division of the images. The dSIR sequence with a narrow mD produces an image that has, in theory, 20 times the  $T_1$  contrast compared to a  $T_1$  FSE sequence.

### 3.5. Echo Subtraction (ES) and Divided Echo Subtraction (dES)

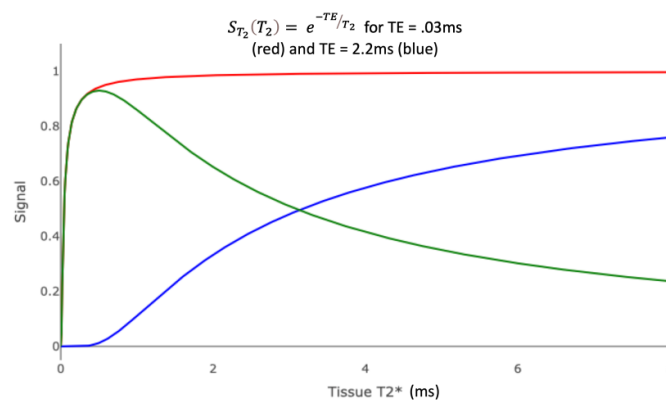
Figure 10a shows the  $T_2^*$  filters for an ultrashort TE sequence with  $TE = 0.03$  ms (red plot) and a short TE sequence with  $TE = 2.2$  ms (blue plot). Cortical bone has a  $T_2^*$  of 0.3 ms and fascia has a  $T_2^*$  of 1–2 ms. The green curve in Figure 10b is the subtraction of the blue

curve from the red curve and is the ES  $T_2^*$  filter. The ES image shows a low to intermediate signal from cortical bone but a high signal from tissues with a  $T_2^*$  similar to fascia. This provides a contrast with longer  $T_2^*$  tissues whose signal is suppressed.

(a)



(b)



(c)

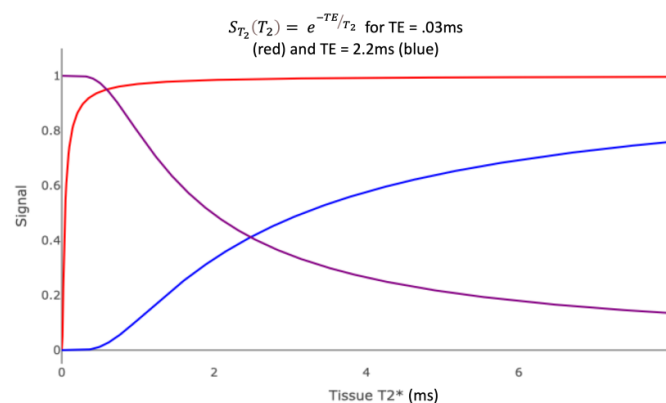


**Figure 10.** Divided echo subtraction (dES)  $T_2^*$  tissue filters. (a)  $T_2^*$  filter for ultrashort and short TE sequences. The red curve is for an ultrashort TE sequence with TE = 0.05 ms. The blue curve is for a short TE sequence with TE = 2.2 ms. (b)  $T_2^*$  filter for the echo subtraction (ES) sequence. The green curve is the difference of the red and blue curves from (a). The subtraction increases the contrast between ultrashort  $T_2^*$  tissues and short/normal  $T_2^*$  tissues. (c)  $T_2^*$  filter for divided echo subtraction (dES) sequence. The purple curve is the difference of the red and blue curves divided by their sum. The dES filter further increases the contrast between ultrashort  $T_2^*$  tissues and short/normal  $T_2^*$  tissues.

The purple curve in Figure 10c is the division of the difference of the red and blue curves by their sum and is the dES  $T_2^*$  filter. In the low ultrashort  $T_2^*$  range of about zero to 0.3 ms, the signal from the dES filter is much higher than that from the ES filter.

#### 4. Clinical Experience with dSIR

Our experience with dSIR is limited to case reports and small case-control studies, but the results are striking, and we believe there is potential for this technique to change how white matter diseases are imaged.

It was initially noticed that dSIR identifies multiple sclerosis (MS) plaques not seen on conventional  $T_2$ -FLAIR images (Figure 11), despite  $T_2$ -FLAIR being a principal part of the gold standard for such imaging. Most pathology in white matter, including edema, ischemia, and demyelinating plaque, results in increases in white matter  $\rho_m$ ,  $T_1$ , and  $T_2$ . In this instance, the increased  $T_2$  in the plaque is insufficient to result in contrast on the  $T_2$ -FLAIR images, but the small increase in white matter  $T_1$  is detected on dSIR images. It was originally thought that dSIR could be used to detect plaques occult on  $T_2$ -FLAIR. This might be useful, because the typical imaging findings in MS are focal, and disease progression is monitored by serial evaluation of the size and characteristics of plaques. Unfortunately, the presence of high signal boundaries makes this difficult. Plaques can masquerade as gray matter, and the immediately subcortical regions are difficult to visualize (Figure 12). It is also not obvious that the ability to simply identify more white matter plaques would make a difference in how MS is diagnosed, staged, and followed.

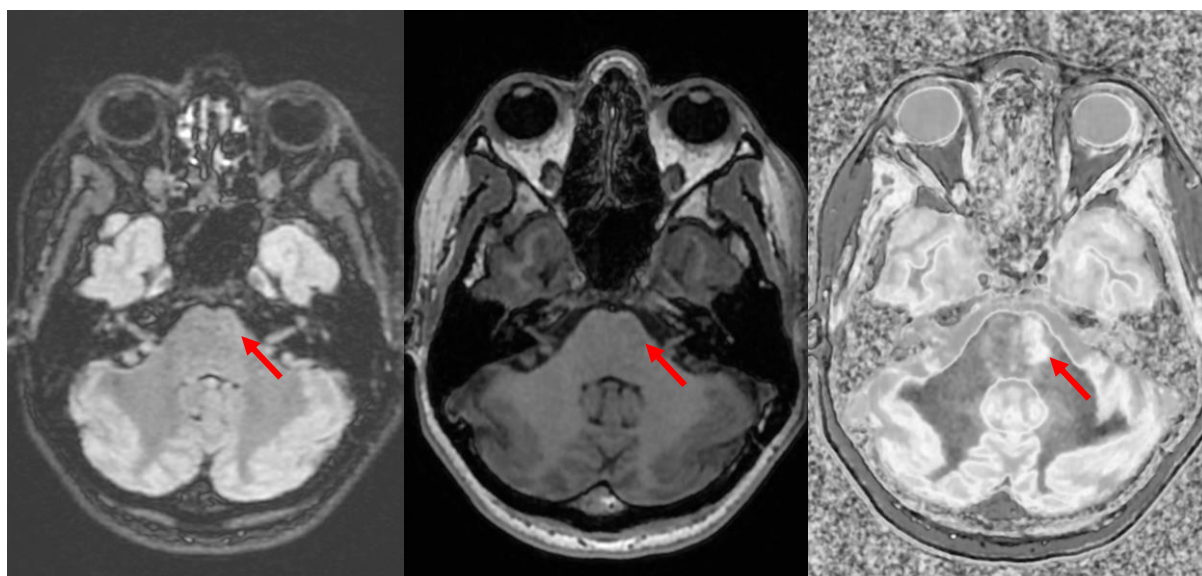


**Figure 11.** Divided Subtracted Inversion Recovery (dSIR) in a patient with multiple sclerosis (MS).  $T_2$ -FLAIR (left), inversion recovery (IR)  $T_1$ -weighted (middle), and wide-domain dSIR with  $TI_{\text{short}} = 450$  ms and  $TI_{\text{long}} = 850$  ms (right) images through the pons in a patient with MS. A large plaque is obviously present in the left hemipons on the dSIR image (red arrow in the image on the far right). The contrast in this image is due to changes in white matter  $T_1$ . The change in  $T_1$  is insufficient to cause noticeable contrast on the IR  $T_1$  image (middle). The change in  $T_2$  is insufficient to cause noticeable contrast on the  $T_2$ -FLAIR image (left).

However, MS is a systemic disease of the white matter. Imaging early and potentially reversible changes in the white matter using dSIR could potentially change the way MS is imaged. In one MS patient having an acute decompensation, the narrow mD dSIR images show geographic, as opposed to focal, changes in the white matter (Figure 13). We do not have a longitudinal follow-up, nor do we have sufficient patients at our institution to perform a longitudinal study. However, collaborators at larger institutions are planning to study this.

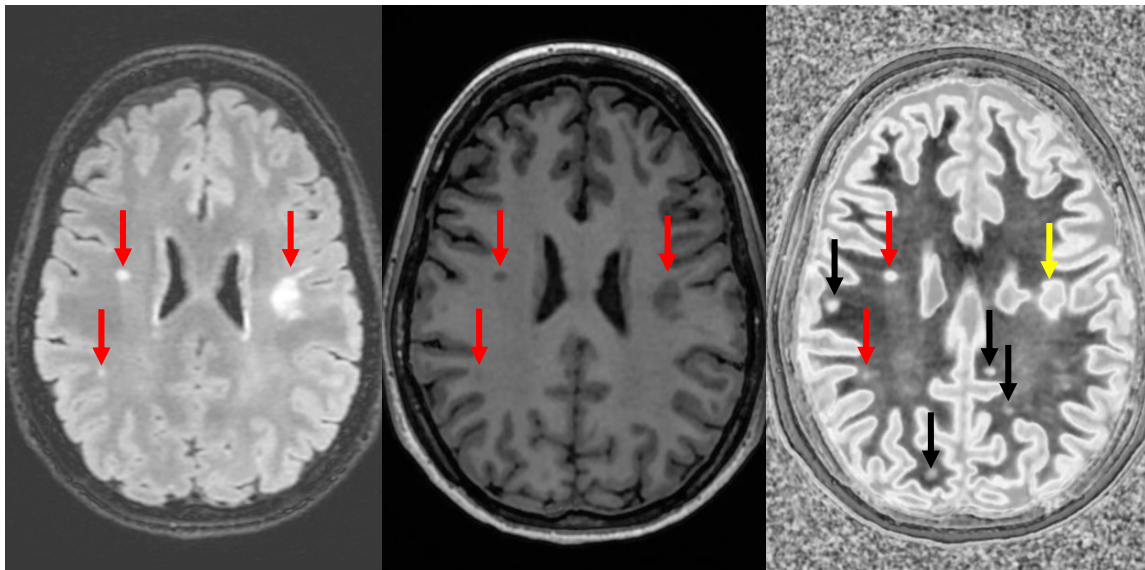


**Figure 12.** Divided Subtracted Inversion Recovery (dSIR) in a patient with multiple sclerosis (MS). T2-FLAIR (**left**), inversion recovery (IR) T<sub>1</sub>-weighted (**middle**), and wide-domain dSIR with T<sub>Ishort</sub> = 450 ms and T<sub>Ilong</sub> = 850 ms (**right**) images through the upper corona radiata in a patient with MS. Three plaques are seen on the T<sub>2</sub>-FLAIR and IR T<sub>1</sub> images (red arrows). More plaques are seen on the dSIR image (black arrows). The plaque in the left frontal white matter is seen on the dSIR image (yellow arrow) but, due to the high signal etching along its margins, could easily be mistaken for cortex.

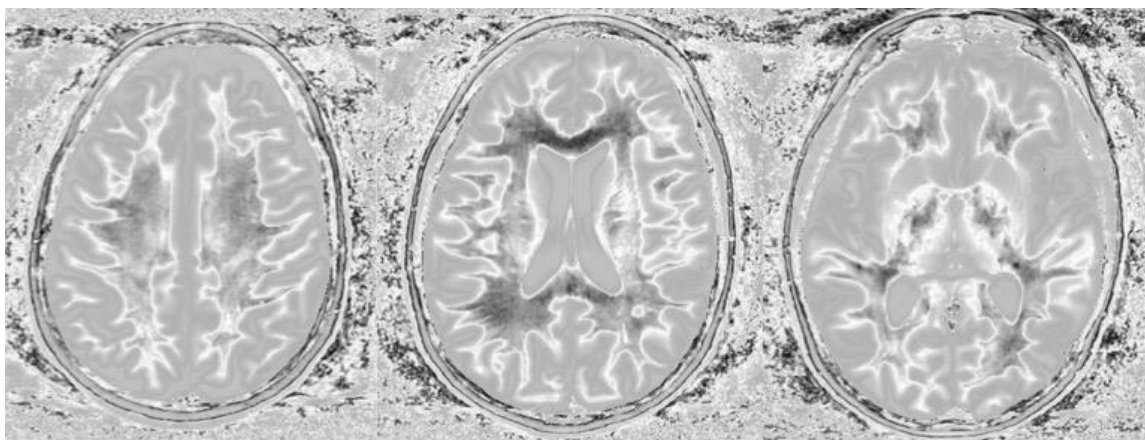


**Figure 13.** Divided Subtracted Inversion Recovery (dSIR) in a patient with multiple sclerosis (MS). Three axial narrow middle domain images in a patient with an acute MS flare at the level of the centrum semiovale (**left**), corona radiata (**middle**), and basal ganglia (**right**). T<sub>Ishort</sub> = 350 ms. T<sub>Ilong</sub> = 500 ms. TE = 7 ms, TR = 5000 ms. The white matter is not black as in Figure 9b. There is a widespread increased signal, though not a “white out” sign as described in Figure 14. This is an “intermediate” appearance but not considered normal.

We believe that dSIR is well suited to identifying generalized changes in white matter T<sub>1</sub>. We have described the “white out sign” as dSIR findings of a widespread and relatively homogeneous high signal throughout the white matter (Figure 14). This contrasts with normal, predominantly low-signal white matter. A third category of a widespread, less increased signal represents an intermediate form of the white out sign.

We have used dSIR to identify acute and chronic generalized white matter changes otherwise occult on clinical imaging. In two patients with suspected delayed post-hypoxic ischemic leukoencephalopathy (Grinker’s myelinopathy), dSIR demonstrated widespread

increased white matter  $T_1$ , despite a normal appearance of the white matter on  $T_2$ -FLAIR images (Figures 15 and 16) [26]. Both patients had experienced prolonged hypoxia due to attempted suicide. One was due to a drug overdose, and the other was due to asphyxia. Scans were obtained nine months and two years following injury. Grinker's has been considered a rare disease, because conventional imaging is typically normal. The disorder may not be as rare as originally thought. dSIR could show obvious findings in symptomatic patients with previously normal conventional  $T_2$ -FLAIR images.

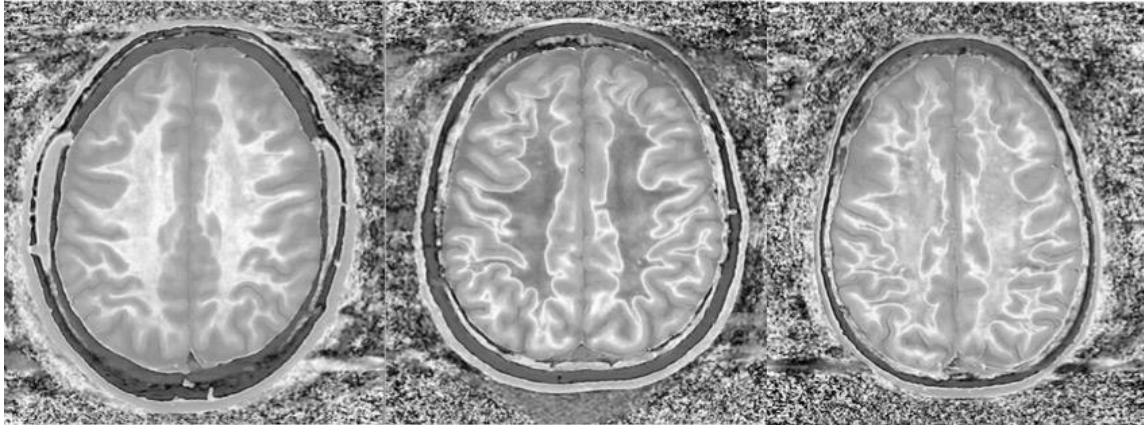


**Figure 14.** Normal and abnormal divided Subtracted Inversion Recovery (dSIR) images. Narrow middle domain images in three patients at the level of the centrum semiovale.  $TI_{short} = 350$  ms.  $TI_{long} = 500$  ms.  $TE = 7$  ms,  $TR = 5000$  ms. The left image shows an example of the “white out sign”, with a diffusely increased signal throughout the white matter. The center image is an example of normal. The white matter has a mildly increased signal that is normal because  $TI_{short} = 350$  ms nulls tissue with  $T_1$  values less than that of white matter. The image on the right has an intermediate appearance, probably abnormal but not a “white out”.

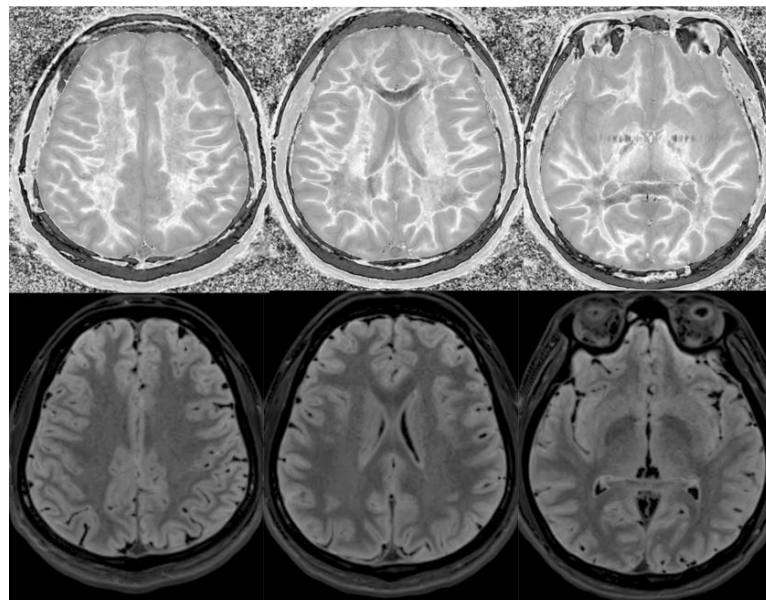


**Figure 15.** Divided Subtracted Inversion Recovery (dSIR) in a patient with Grinker's myelinopathy. **Top row:** Narrow middle domain dSIR images at the level of the centrum semiovale (**left**), corona radiata (**middle**), and basal ganglia (**right**) in a patient with persistent symptoms following prolonged hypoxia due to a suicide attempt.  $TI_{short} = 350$  ms.  $TI_{long} = 500$  ms.  $TE = 7$  ms,  $TR = 5000$  ms. There is a diffuse “white out”. **Bottom row:**  $T_2$ -FLAIR images at matching levels show normal-appearing white matter. Scans were obtained 9 months following injury.

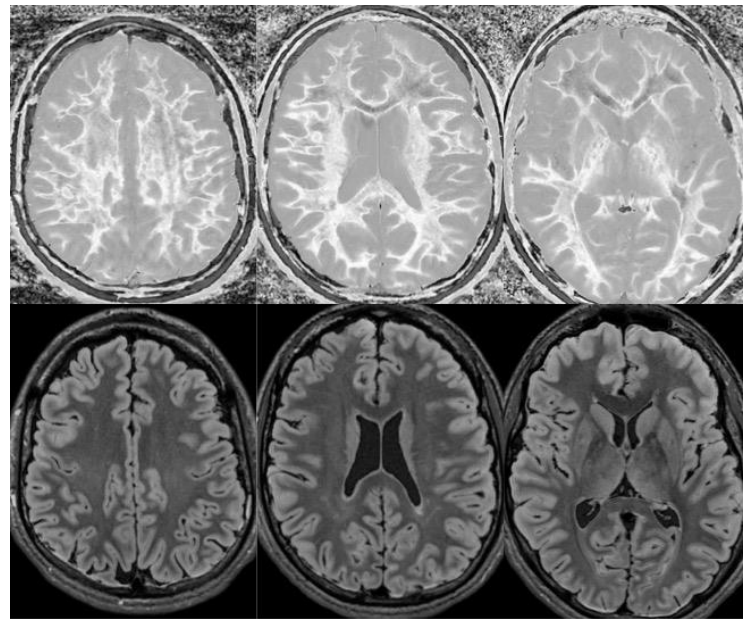


**Figure 16.** Divided Subtracted Inversion Recovery (dSIR) in a patient with Grinker's myelinopathy. **Top row:** Narrow middle domain dSIR images at the level of the centrum semiovale (**left**), corona radiata (**middle**), and basal ganglia (**right**) in a patient with persistent symptoms following prolonged hypoxia due to drug overdose.  $TI_{\text{short}} = 350$  ms.  $TI_{\text{long}} = 500$  ms.  $TE = 7$  ms,  $TR = 5000$  ms. There is widespread "white out", with some sparing in the deep frontal lobe white matter. **Bottom row:** T<sub>2</sub>-FLAIR images at matching levels show normal-appearing white matter. Scans were obtained 2 years following injury.

In another example, a matched pair of scans in two teenage boys with impact-related head injury in the same rugby match showed widespread white matter changes in the symptomatic player but not in the asymptomatic one (Figure 17).

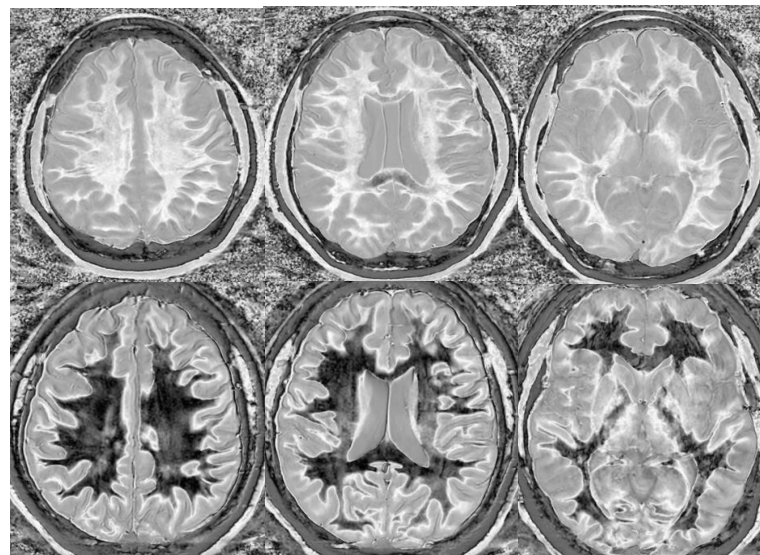


**Figure 17.** Two boys with mild head trauma. **Top row:** Narrow middle domain divided Subtracted Inversion Recovery (dSIR) images at the level of the centrum semiovale (**left**), corona radiata (**middle**), and basal ganglia (**right**) in two young men experiencing mild head trauma in the same rugby match.  $TI_{\text{short}} = 350$  ms.  $TI_{\text{long}} = 500$  ms.  $TE = 7$  ms,  $TR = 5000$  ms. Images were obtained within 5 days of injury. The player shown in the **top row** had symptoms of concussion at the time of imaging, and a "white out" sign is present. The player shown in the **bottom row** was asymptomatic, and the images appear normal.

In a case–control cohort currently being prepared for journal submission, 27 of 33 patients with chronic post-concussive symptoms, clinically selected for being at high risk of having a brain abnormality, had a “white out” sign on dSIR images. The remaining five had intermediate findings. The T<sub>2</sub>-FLAIR showed no diffuse abnormalities in all 33 patients. An unmatched cohort of normal volunteers had normal white matter. Case–control studies do not prove correlation, and we are in the process of organizing a prospective study on acute mTBI patients to correlate the white matter changes seen on dSIR with the clinical course of symptoms.

Particularly encouraging, however, is anecdotal evidence that generalized white matter changes detected with dSIR sequences are reversible. Imaging in a patient following chronic methamphetamine use showed widespread white matter changes, which resolved following a prolonged period of abstinence (Figure 18). A similar reversibility was seen in a symptomatic patient following an mTBI (Figure 19). Imaging in the days following injury showed diffuse white matter changes which, along with the symptoms, resolved within two weeks.

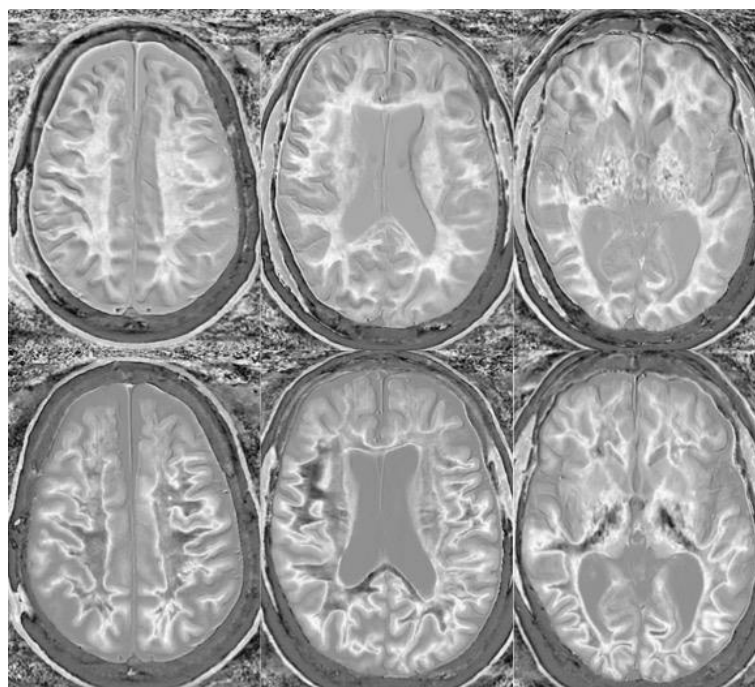


**Figure 18.** Divided Subtracted Inversion Recovery (dSIR) in a patient methamphetamine user. Narrow middle domain dSIR images at the level of the centrum semiovale (**left**), corona radiata (**middle**), and basal ganglia (**right**) in a volunteer immediately after a methamphetamine binge (**top row**) and 4 months into abstinence (**bottom row**)  $TI_{short} = 350$  ms.  $TI_{long} = 500$  ms.  $TE = 7$  ms,  $TR = 5000$  ms. The **top row** images show the “white out” sign, indicating diffuse mild white matter T<sub>1</sub> elevation. The signal in the white matter partially normalizes on the bottom row. The appearance is closer to intermediate than normal, but there is definite improvement.

If dSIR can detect acute reversible changes in patients having acute MS flares, then it could be used as an imaging biomarker for treatment response. If reversible white matter changes consistently correlate with symptoms in mTBI, then imaging could be used to identify patients suffering damage from head trauma and possibly predict early recovery. In addition, demonstrating chronic white matter changes in patients with chronic symptoms but negative imaging provides an objective validation of disease. This is empowering for patients who have been told there is “nothing wrong with them”. It also provides a basis for funding treatment. Prospective trials need to be performed, but preliminary results suggest there is promise for using dSIR to detect subtle changes in white matter following

insults to the brain. There is also potential for dSIR to play a similar role in post-viral syndromes such as long COVID.

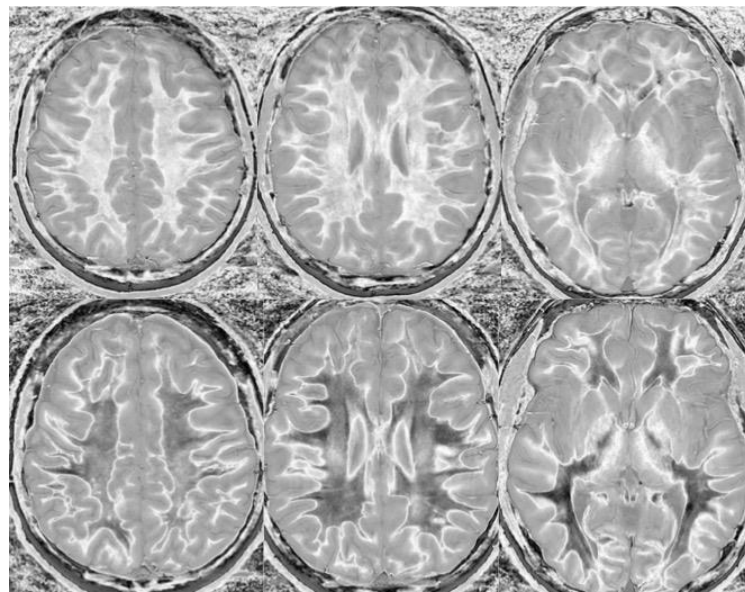


**Figure 19.** Divided Subtracted Inversion Recovery (dSIR) in a patient with a mild traumatic brain injury. Narrow middle domain dSIR images at the level of the centrum semiovale (**left**), corona radiata (**middle**), and basal ganglia (**right**) in a volunteer within five days of an mTBI (**top row**) and two weeks later (**bottom row**).  $TI_{short} = 350$  ms.  $TI_{long} = 500$  ms.  $TE = 7$  ms,  $TR = 5000$  ms. The **top row** images show the “white out” sign, indicating diffuse mild white matter  $T_1$  elevation. The signal in the white matter normalizes on the bottom row, where it appears normal.

dSIR is not limited to detecting changes in white matter.  $TI_{short}$  and  $TI_{long}$  can be chosen to maximize sensitivity to changes in tissue  $T_1$  between any two  $T_1$  values—hence, the term targeted MRI (tMRI). In Figure 8c,  $TI_{short}$  and  $TI_{long}$  are chosen to show small changes in gray matter  $T_1$ . It would be interesting to compare this sequence with MP2RAGE and FLAWS hc for detecting cortical plaques in MS. MR fingerprinting has suggested that the primary difference between normal prostate tissue and prostate cancer is a decrease in tissue  $T_1$  [27]. However, differences in  $T_1$  between normal and cancerous tissues in the prostate are insufficient to produce contrast on standard FSE or IR  $T_1$ -weighted FSE sequences. If  $TI_{long}$  is chosen to null normal peripheral zone prostate tissue and  $TI_{short}$  is chosen to null tissue with a shorter  $T_1$ , normal peripheral zone tissue will appear bright and prostate cancers should appear dark. A proof of concept has been performed in normal volunteers [28]; however it is unknown if this approach will add specificity to the current techniques, which rely instead on  $T_2$  and  $D^*$  for differentiating prostate cancer from normal background tissue.

dSIR images are created from the pixel-by-pixel division of the difference of two standard IR images by their sum. These types of IR sequences are available on most clinical MR systems. The straightforward image arithmetic is easily performed using a MATLAB script. Technical barriers for implementation are therefore low.

### 5. Practical Limitations of dSIR and Future Technical Modifications

As implemented above, the dSIR sequence is not a high-resolution technique. The examples shown in Section 4 of the manuscript used a 2D fast spin echo technique, with 4 mm slices and an in-plane resolution of  $1 \times 1$  mm. This is appropriate for detecting wide-spread changes in the white matter but may be limited for detecting small, focal changes, especially in the subcortical regions, where there is a high signal boundary between white and gray matter. The technique can also be performed using 3D high-resolution-magnetization-prepared gradient echo inversion recovery sequences, which

can produce images with an isotropic 0.7 mm (or less) resolution. This is preferable for reducing artifacts due to volume averaging or when looking for focal abnormalities. The gradient echo readout modifies Equation 8, and the choices of  $TI_{short}$  and  $TI_{long}$  require mild modification.

There are also inherent limitations when performing analyses on images obtained at two separate time points. Even subtle patient motion between the two IR acquisitions will result in misregistration during the image arithmetic, resulting in artifacts on the dSIR images. Motion correction techniques such as radial/propeller/blade k-space trajectories in the data space, combined with rigid image registration techniques in the image space, can be used to correct for small amounts of motion prior to subtraction and division. These extra steps may limit the ability of older MR systems to create dSIR images. Our experience is that misregistration is uncommon in most patients.

dSIR images are also not intended to be viewed in isolation. The limited range of tissue  $T_1$ s where there is image contrast means that large changes in tissue  $T_1$ , or changes outside the mD, are missed. We therefore always review the dSIR images beside conventional  $T_2$ -FLAIR and  $T_2$  images. This is especially important when looking for focal, as opposed to widespread, changes.

dSIR is inherently a targeted technique. The range of evaluated tissues is defined by the user through the choice of  $TI_{short}$  and  $TI_{long}$ . This requires accurate knowledge of the  $T_1$  values of the tissues of interest, which is not always the case. If the  $TI_{short}$  chosen is too high then small changes in normal white matter  $T_1$  can result in a decreased, not increased, signal (Figure 20). The width of the mD is also critically important. If the mD is too wide, then the slope of the  $T_1$  bipolar filter in the mD may be insufficient to show subtle changes in  $T_1$ . If the pathologic changes in  $T_1$  are larger than the width of the mD, then the findings can be less obvious, because the slopes of the dSIR  $T_1$  filters in Figure 8a,b become negative above the maximum  $T_1$  of the mD, which results in less increase in signal and lower contrast.

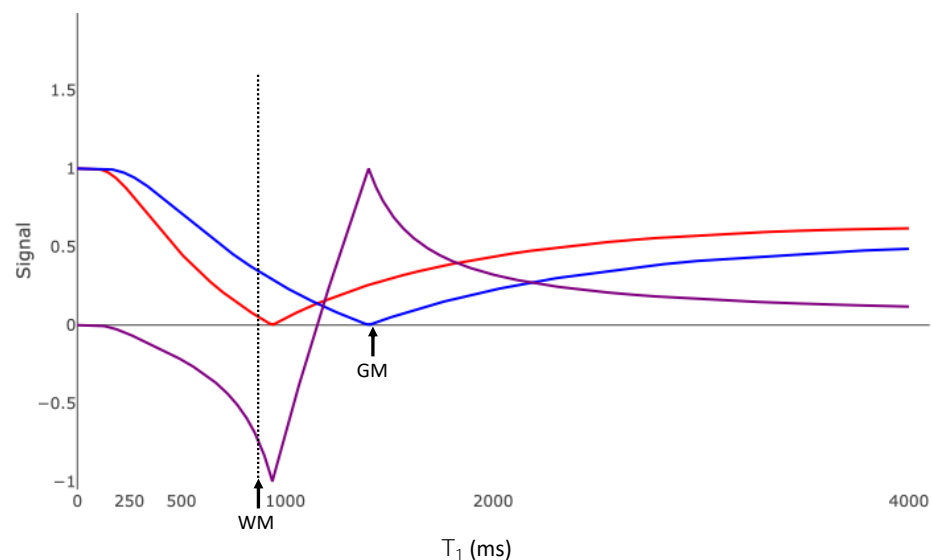


**Figure 20.** Divided Subtracted Inversion Recovery (dSIR)  $T_1$  filter with the shorter inversion time chosen too high. The red and blue curves are the  $T_1$  filters for IR sequences designed to null white (red curve) and gray (blue curve) matter. The TI for the red curve has been chosen too high. Small increases in  $T_1$  from normal in the white matter will result in decreased as opposed to increased signal on the dSIR filter (purple curve). GM— $T_1$  value of gray matter. WM— $T_1$  value of white matter.

There are at least two approaches to targeting dSIR sequences. The first is to implement dSIR with a specific mD that accommodates variations in the normal  $T_1$  of white matter and allows for intermediate, as well as small, increases in white matter  $T_1$ . This is our current approach with dSIR imaging. The TR is chosen long compared to the  $T_1$  of the

tissues, typically around 5000 ms. When dividing the difference of the images by their sum, the  $T_2$  and  $\rho_m$  filters cancel, so the choice of TE in theory is arbitrary, though we choose a low TE = 7 ms to definitely remove  $T_2$  weighting from the process. Initial values for  $TI_{short}$  and  $TI_{long}$  were chosen in an attempt to accurately null white and gray matter, respectively, based on both the published values of gray and white matter  $T_1$  at 3T and also our experience using various inversion times on normal volunteers. However, we found that attempting to accurately null white matter resulted in many scans where the  $TI_{short}$  was a little too long, and the multiple attempts at accurately identifying  $TI_{short}$  resulted in long examination times. We ultimately chose  $TI_{short} = 350$  ms and  $TI_{long} = 500$  ms for studying generalized disease in the white matter.  $TI_{short} = 350$  ms is below the value needed to null normal white matter but ensures that any increases in white matter  $T_1$  from normal will result in an increased signal. This results in normal white matter often having a mildly increased signal. The mD is narrow enough to ensure the steep slope of the  $T_1$  filter in the mD but wide enough to allow for a range of white matter increases in  $T_1$ . The advantage of this approach is that useful dSIR imaging can be made available on virtually all clinical MRI scanners using existing IR sequences, without requiring close attention to sequence parameters. The scan time is short (both 2D and 3D data sets can be acquired in approximately five minutes), and the post-processing involves simple image arithmetic.

The second approach is to obtain dSIR images with a wide mD and mathematically create narrower mD images. The dSIR filter is approximately linear between the  $T_1$  values of the tissues nulled by  $TI_{short}$  and  $TI_{long}$  (Figures 8a,b and 20). Within the mD, the signal of the  $T_1$  filter is approximated by the equation

$$S_{dSIR} = \frac{\ln 4}{TI_{long} - TI_{short}} \times T_1 - \frac{TI_{long} + TI_{short}}{TI_{long} - TI_{short}} \quad (9)$$

Solving for  $T_1$  turns the dSIR image into a  $T_1$  map, which can be used in Equation (8) to mathematically create images for any  $TI_{long}$  and  $TI_{short}$  that fall within the mD of the original dSIR image. A synthetically created narrow mD dSIR image can then be computed. If  $TI_{short}$  and  $TI_{long}$  are initially chosen to encompass gray and white matter, then synthetic images can be optimized to the  $T_1$  values for gray and white matter for each patient. Unfortunately, this has proved difficult to accomplish, because it is not clear how to identify the  $T_1$  of “normal” white matter in cases of widespread disease.

The ability to create  $T_1$  maps from the dSIR images suggests two additional limitations of the technique. First, if dSIR images can be created mathematically from  $T_1$  maps, then why bother to obtain the two IR sequences if a  $T_1$  map is already available? This is a valid criticism. Standard IR sequences are readily available on most clinical MRI systems, but high-resolution  $T_1$ -mapping techniques are not. The MP2RAGE sequence creates a  $T_1$  map encompassing all tissues on the image and is becoming increasingly common on clinical systems. The FLAWShc sequence can also be used to create a  $T_1$  map using a very wide mD. (FLAWShc could be considered a very wide mD dSIR technique but does not use magnitude reconstruction and does not produce a bipolar  $T_1$  filter).  $T_1$  maps created from both these sequences could be used to synthetically create subsequent images targeted at specific tissues. However, we believe that the more closely a range of  $T_1$  values are targeted by the original acquisition, the more accurate the subsequent  $T_1$  map will be. When looking for small changes in  $T_1$ , we want to use the most accurate technique available. Starting with a smaller, targeted mD may result in more accurate  $T_1$  maps for the tissues we want to evaluate. A comparison of these different  $T_1$ -mapping techniques for the creation of dSIR images will need to be performed.

The second limitation is that the information contained on the dSIR image is essentially a linear mapping of  $T_1$  values to pixel brightness. If a simple  $T_1$  map of the tissues in the mD were available, then an equivalent image could be generated by creating an image lookup table having the same shape as the bipolar  $T_1$  filter in Figure 8a,b. dSIR encodes the contrast into the image data, which can be shared and viewed on any image viewer. The lowest signal corresponds to the tissue nulled by  $TI_{short}$ , and the highest signal corresponds to the

tissue nulled by  $T_{1\text{long}}$ . It is straightforward to view the images using a full-dynamic-range linear gray scale lookup table which is available on all image viewers (specifically DICOM image viewers for medical images). It is not straightforward to design a bipolar, gray scale lookup table and import it into a viewer of choice. From this perspective, generating the dSIR image (either directly or synthetically) and encoding the contrast in the image file is more practical.

An additional limitation of the dSIR sequence as implemented for white matter is that the etiology of the small changes in  $T_1$  is unknown and may include other pathological processes besides neuroinflammation, including edema, demyelination, and degeneration. We have hypothesized that subtle neuroinflammation results in  $T_1$  increases too small to detect with conventional FSE and IR sequences. Whether this is accompanied by small increases in  $T_2$  is unknown, but frequently in disease, increases in  $T_1$  are accompanied by increases in  $T_2$ . We are currently seeking funding to test dSIR in an animal model with histology as a reference standard. If dSIR is a marker of subtle neuroinflammation, then there is potential to use dSIR to triage mTBI patients who would benefit from anti-inflammatory therapies.

## 6. Future Validation

dSIR is an emerging technique and, despite the preliminary evidence presented above, has not undergone clinical validation. Prospective studies on symptomatic patients need to be performed to establish a correlation between symptoms, recovery, and white matter changes. This needs to be done separately for diseases like acute and chronic mTBI, MS, long COVID, and other post-viral syndromes. Histologic correlations need to be performed to determine the specific etiology of white matter changes. Prospective studies comparing dSIR to imaging techniques in other parts of the body also need to be performed. Examples include comparing dSIR to MP2RAGE and FLAWS hc for detecting cortical plaques in MS, and comparing dSIR to high b-value diffusion-weighted images for detecting cancers in the peripheral zone of the prostate.

## 7. Research Experience with dES

Musculoskeletal MRI as a field has primarily concerned itself with skeletal, joint, and muscular imaging. With improved imaging, we can advance our knowledge of tendon and fascial pathologies [28–30]. We have used dES to generate high-spatial-resolution images of the upper and lower extremities, with a high contrast between tendons/fascia/aponeurosis and the surrounding soft tissues. These images are incorporated into pipelines for creating finite-element models of the musculoskeletal system [31,32] which can simulate anatomical function [33,34]. dES and subtraction techniques using UTE sequences allow the novel visualization of fascia in vivo to understand anatomical variation in populations, explore its potential role in disease, and build realistic models to explore its role in musculoskeletal phenomena that are poorly understood [35].

On an ultrashort TE image acquired with  $TE = 0.03$  ms, the cortical bone and fascia are dark and longer  $T_2^*$  tissues are bright (Figure 21a). Inverting the gray scale creates a “CT”-like image of the cortical bone (Figure 21b, also see Figure 1). Aponeuroses are also bright, but contrast with the surrounding soft tissues is low. The fascial planes are not well delineated. An ES image created by subtracting a  $TE = 2.2$  ms image from a  $TE = 0.03$  ms image (Figure 21c) shows increased contrast between the connective tissues and adjacent soft tissues due to increased suppression of the higher  $T_2$  tissues, which appear darker than in Figure 21b. The fascial planes are better delineated than on the inverted images. Cortex is not bright as predicted by the green curve in Figure 10b. A dES image created from  $TE = 0.03$  ms and  $TE = 2.2$  ms images shows increased contrast between the ultrashort  $T_2$  tissues and the background tissues. Fascial planes and aponeuroses are well visualized.

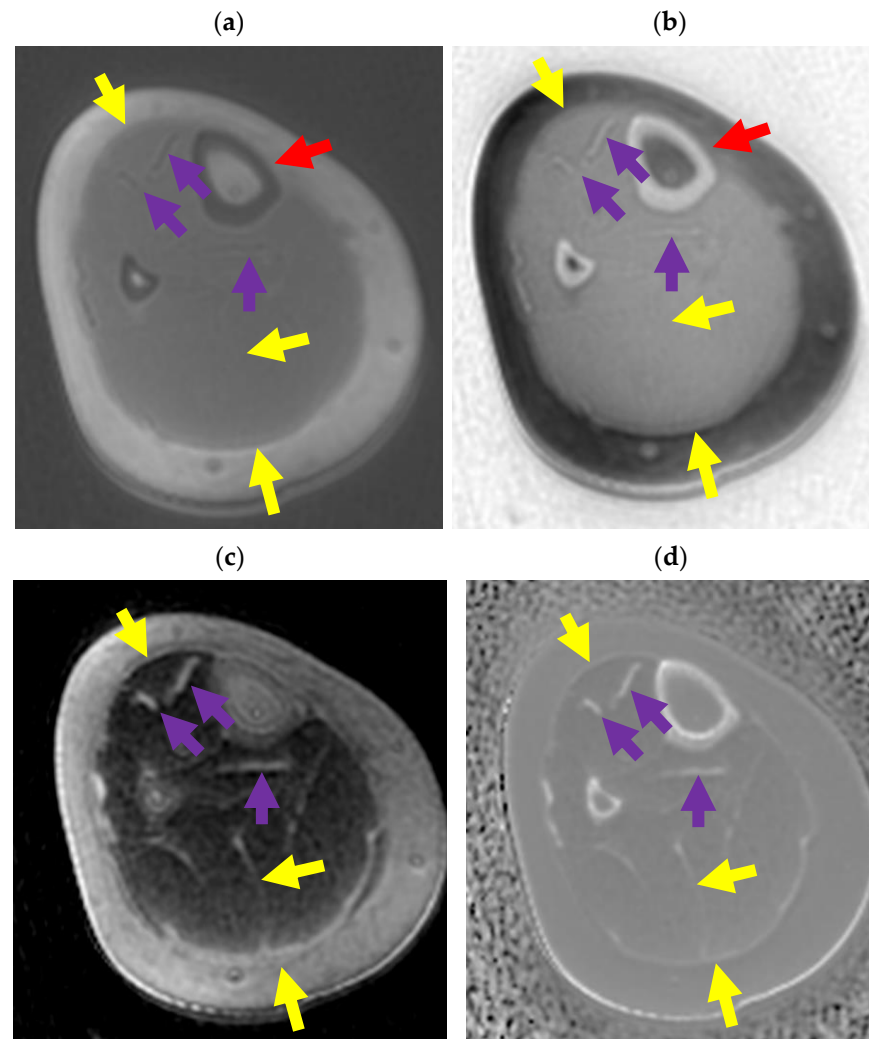


**Figure 21.** Divided echo subtraction (dES) (a) Axial ultrashort TE image through the lower leg with TE = 0.03 ms. Cortical bone (red arrows), and aponeuroses (purple arrows) are dark. The fascial layers (yellow arrows) are thin and poorly seen. (b) The same axial ultrashort TE image through the lower leg as in (a) displayed with an inverted gray scale. Cortical bone (red arrows) and aponeuroses (purple arrows) are bright. The fascial layers (yellow arrows) are thin and poorly seen. (c) Axial ES image created by subtracting a TE = 2.2 ms image from the TE = 0.03 ms image. The contrast between aponeuroses (purple arrows), fascia (yellow arrows), and muscle is increased compared to (b). (d) Axial dES image created by dividing the difference of the TE = 2.2 ms and TE = 0.03 ms images by their sum. The contrast between aponeuroses (purple arrows), fascia (yellow arrows), and muscle is improved compared to (b,c).

Imaging fascia in the extremities is technically challenging. There are at least three different tissue types in close proximity (short  $T_2$  fascia/aponeuroses, fat—which contains both long and short  $T_2$  components, and skeletal muscle). This type of imaging is prone to chemical shift artifacts and remains a work in progress. However, it serves as a practical example of using division and subtraction to increase soft tissue contrast.

## 8. Summary

Division and subtraction is a novel way of generating ultrahigh  $T_1$  and  $T_2$  contrast from otherwise basic and readily available MRI pulse sequences. The dSIR sequence produces  $T_1$ -weighted images that are, in theory, 20 times more sensitive than traditional SE  $T_1$ -weighted images for detecting small changes in  $T_1$  from normal. We currently use dSIR to identify widespread changes in white matter  $T_1$  in mTBI, MS, and other diffuse

brain disorders. To our knowledge, no other conventional or advanced MRI technique can do this. Because dSIR can be targeted to be sensitive to  $T_1$  changes from normal within any tissue, we also plan to explore its utility in imaging prostate cancer. The dES sequence produces a similarly increased  $T_2$ -weighted contrast for imaging short  $T_2$  tissues.

**Author Contributions:** Conceptualization, D.C., P.C., M.B., E.K. and G.B.; Data curation, P.C., J.M., M.S., G.H., M.R.P. and E.K.; Funding acquisition, S.H.; Methodology, D.C., P.C., G.N., J.M., M.S., M.G., G.H., M.R.P., T.M., E.K. and G.B.; Project administration, S.H.; Software, D.C., P.C. and M.B.; Supervision, D.C., S.H., E.K. and G.B.; Validation, G.N., J.M. and M.S.; Writing—original draft, D.C.; Writing—review and editing, D.C., P.C., G.N., J.M., M.B., M.G., G.H., T.M. and G.B. All authors have read and agreed to the published version of the manuscript.

**Funding:** This research was funded by the Fred Lewis Enterprise Foundation, the Hugh Green Foundation, Manaaki Moves Trust, the JN & HB Williams Foundation, the Mangatawa Beale Williams Memorial Trust, Anonymous Donor, an Agility Grant from the Wu Tsai Human Performance Alliance, Friends of Mātai Blue Sky Fund, and Kānoa—Regional Economic Development & Investment Unit of New Zealand. We are also grateful for support from GE Healthcare and Mātai Ngā Māngai Māori.

**Institutional Review Board Statement:** The study was conducted in accordance with the Declaration of Helsinki and approved by the Auckland Hospital Research Ethics Committee (approval number AHRECAH1006 in 2021).

**Informed Consent Statement:** Informed consent was obtained from all patients whose images are used in this manuscript.

**Data Availability Statement:** No formal data sets were created as part of this manuscript.

**Conflicts of Interest:** The authors declare no conflicts of interest. The funders had no role in the design of this manuscript.

## References

- Bloch, F. Nuclear induction. *Phys. Rev.* **1946**, *70*, 460–474. [[CrossRef](#)]
- Young, I.R.; Hall, A.S.; Pallis, C.A.; Legg, N.J.; Bydder, G.M.; Steiner, R.E. Nuclear magnetic resonance imaging of the brain in multiple sclerosis. *Lancet* **1981**, *2*, 1063–1066. [[CrossRef](#)] [[PubMed](#)]
- Bailes, D.R.; Young, I.R.; Thomas, D.J.; Straughan, K.; Bydder, G.M.; Steiner, R.E. NMR imaging of the brain using spin-echo sequences. *Clin. Radiol.* **1982**, *33*, 395–414. [[CrossRef](#)] [[PubMed](#)]
- Bydder, G.M.; Steiner, R.E.; Young, I.R.; Hall, A.S.; Thomas, D.J.; Marshall, J.; Pallis, C.A.; Legg, N.J. Clinical NMR imaging of the brain: 140 cases. *AJR Am. J. Roentgenol.* **1982**, *139*, 215–236. [[CrossRef](#)] [[PubMed](#)]
- Crooks, L.E.; Mills, C.M.; Davis, P.L.; Brant-Zawadzki, M.; Hoenninger, J.; Arakawa, M.; Watts, J.; Kaufman, L. Visualization of cerebral and vascular abnormalities by NMR imaging. *Eff. Imaging Parameters Contrast. Radiol.* **1982**, *144*, 843–852.
- Lukes, S.A.; Crooks, L.E.; Aminoff, M.J.; Kaufman, L.; Panitch, H.S.; Mills, C.; Norman, D. Nuclear magnetic resonance imaging in multiple sclerosis. *Ann. Neurol.* **1983**, *13*, 592–601. [[CrossRef](#)] [[PubMed](#)]
- Bydder, G.M.; Young, I.R. MR imaging: Clinical use of the inversion recovery sequence. *J. Comput. Assist. Tomogr.* **1985**, *9*, 659–675. [[CrossRef](#)]
- De Coene, B.; Hajnal, J.V.; Gatehouse, P.; Longmore, D.B.; White, S.J.; Oatridge, A.; Pennock, J.M.; Young, I.R.; Bydder, G.M. MR of the brain using fluid-attenuated inversion recovery (FLAIR) pulse sequences. *AJNR Am. J. Neuroradiol.* **1992**, *13*, 1555–1564.
- Redpath, T.W.; Smith, F.W. Technical note: Use of a double inversion recovery pulse sequence to image selectively grey or white brain matter. *Br. J. Radiol.* **1994**, *67*, 1258–1263. [[CrossRef](#)]
- Marques, J.P.; Kober, T.; Krueger, G.; van der Zwaag, W.; Van de Moortele, P.F.; Gruetter, R. MP2RAGE, a self bias-field corrected sequence for improved segmentation and  $T_1$ -mapping at high field. *Neuroimaging* **2010**, *49*, 1271–1281. [[CrossRef](#)]
- Spini, M.; Choi, S.; Harrison, D.M. 7T MP-FLAIR versus MP2RAGE for Quantifying Lesion Volume in Multiple Sclerosis. *J. Neuroimaging* **2020**, *30*, 531–536. [[CrossRef](#)] [[PubMed](#)]
- Demortière, S.; Lehmann, P.; Pelletier, J.; Audoin, B.; Callot, V. Improved Cervical Cord Lesion Detection with 3D-MP2RAGE Sequence in Patients with Multiple Sclerosis. *AJNR Am. J. Neuroradiol.* **2020**, *41*, 1131–1134. [[CrossRef](#)] [[PubMed](#)]
- Beaumont, J.; Saint-Jalmes, H.; Acosta, O.; Kober, T.; Tanner, M.; Ferré, J.C.; Salvado, O.; Fripp, J.; Gambarota, G. Multi  $T_1$ -weighted contrast MRI with fluid and white matter suppression at 1.5 T. *Magn. Reson. Imaging* **2019**, *63*, 217–225. [[CrossRef](#)] [[PubMed](#)]
- Müller, J.; La Rosa, F.; Beaumont, J.; Tsagkas, C.; Rahmzadeh, R.; Weigel, M.; Cuadra, M.; Gambarota, G.; Granziera, C. Fluid and White Matter Suppression- New Sensitive 3T Magnetic Resonance Imaging Contrasts for Cortical Lesion Detection in Multiple Sclerosis. *Investig. Radiol.* **2022**, *57*, 592–600. [[CrossRef](#)] [[PubMed](#)]

15. Saade, C.; Bou-Fakhredin, R.; Yousem, D.; Asmar, K.; Naffaa, K.; El-Merhi, F. Gadolinium and Multiple Sclerosis: Vessels, Barriers of the Brain, and Glymphatics. *AJNR Am. J. Or Neuroradiology* **2018**, *39*, 2168–2176. [[CrossRef](#)] [[PubMed](#)]
16. Filippi, M.; Rocca, M.A. MRI evidence for multiple sclerosis as a diffuse disease of the central nervous system. *J. Neurol.* **2005**, *252* (Suppl. S5), 16–24. [[CrossRef](#)] [[PubMed](#)]
17. Fan, S.; Ma, Y.; Lv, X.; Du, J.; Bydder, G.M.; Szeverenyi, N.M. Demonstration of abnormal cortical layers in Alzheimer’s disease using subtracted tissue attenuated inversion recovery (STAIR) pulse sequences. In Proceedings of the ISMRM 2017, Honolulu, HI, USA, 22–27 April 2017.
18. Speckter, H.; Bido, J.; Hernandez, G.; Rivera, D.; Suazo, L.; Valenzuela, S.; Fermin, R.; Oviedo, J.; Foerster, B.; Gonzalez, C.; et al. Inversion recovery sequences improve delineation of optic pathways in the proximity of suprasellar lesions. *J. Radiosurgery SBRT* **2018**, *5*, 115–122.
19. Ma, Y.J.; Moazamian, D.; Cornfeld, D.M.; Condrón, P.; Holdsworth, S.J.; Bydder, M.; Du, J.; Bydder, G.M. Improving the understanding and performance of clinical MRI using tissue property filters and the central contrast theorem, MASDIR pulse sequences and synergistic contrast MRI. *Quantitative Imaging Med. Surg.* **2022**, *12*, 4658–4690. [[CrossRef](#)] [[PubMed](#)]
20. Ma, Y.J.; Moazamian, D.; Port, J.D.; Edjlali, M.; Pruvo, J.P.; Haccin-Bey, L.; Hoggard, N.; Paley, M.N.J.; Menon, D.K.; Bonekamp, D.; et al. Targeted magnetic resonance imaging (tMRI) of small changes in the T1 and spatial properties of normal or near normal appearing white and gray matter in disease of the brain using divided subtracted inversion recovery (dSIR). *Quantitative Imaging Med. Surg.* **2023**, *13*, 7304–7337. [[CrossRef](#)]
21. Breighner, R.E.; Potter, H.G. CT-like Contrast for Bone Imaging with ZTE-MRI. In *MRI of Short- and Ultrashort-T2 Tissues. Making the Invisible Visible*; Du, J., Bydder, G., Eds.; Springer: Berlin/Heidelberg, Germany, 2024; pp. 549–560.
22. Wiesinger, F.; Sacolick, L.I.; Menini, A.; Kaushik, S.S.; Ahn, S.; Veit-Haibach, P.; Delso, G.; Shanbhag, D.D. Zero TE MR bone imaging in the head: Zero TE bone imaging. *Magn. Reson. Med.* **2016**, *75*, 107–114. [[CrossRef](#)]
23. Ma, Y.-J.; Zhu, Y.; Lu, X.; Carl, M.; Chang, E.Y.; Du, J. Short T2 imaging using a 3D double adiabatic inversion recovery prepared ultrashort echo time cones (3D DIR-UTE-cones) sequence. *Magn. Reson. Med.* **2018**, *79*, 2555–2563. [[CrossRef](#)] [[PubMed](#)]
24. Condrón, P. Imaging Fascia. Acquisition & Post Processing Including MASDEA (Multiplied, Added, Subtracted & Divided Echo Acquisition). In Proceedings of the ISMRT, Toronto, ON, Canada, 3–8 June 2023.
25. Young, I.R.; Szeverenyi, N.M.; Du, J.; Bydder, G.M. Pulse sequences as tissue property filters (TP-filters): A way of understanding the signal, contrast and weighting of magnetic resonance images. *Quantitative Imaging Med. Surg.* **2020**, *10*, 1080–1120. [[CrossRef](#)] [[PubMed](#)]
26. Newburn, G.; Condrón, P.; Kwon, E.E.; McGeown, J.P.; Melzer, T.R.; Bydder, M.; Griffin, M.; Scadeng, M.; Potter, L.; Holdsworth, S.J.; et al. Diagnosis of Delayed Post-Hypoxic Leukoencephalopathy (Grinker’s Myelinopathy) with MRI Using Divided Subtracted Inversion Recovery (dSIR) Sequences: Time for Reappraisal of the Syndrome? *Diagnostics* **2024**, *14*, 418. [[CrossRef](#)] [[PubMed](#)]
27. Lo, W.; Panda, A.; Juang Yun Ahad, J.; Gulani, V.; Siberlich, N. MR Fingerprinting of the Prostate. *Magn. Reson. Mater. Phys. Biol. Med.* **2022**, *35*, 557–571. [[CrossRef](#)] [[PubMed](#)]
28. Kondrup, F.; Gaudreault, N.; Venne, G. The deep fascia and its role in chronic pain and pathological conditions: A review. *Clin. Anat.* **2022**, *35*, 649–659. [[CrossRef](#)] [[PubMed](#)]
29. Klingler, W.; Velders, M.; Hoppe, K.; Pedro, M.; Schleip, R. Clinical relevance of fascial tissue and dysfunctions. *Curr. Pain Headache Rep.* **2014**, *18*, 1–7. [[CrossRef](#)] [[PubMed](#)]
30. Liptan, G.L. Fascia: A missing link in our understanding of the pathology of fibromyalgia. *J. Bodyw. Mov. Ther.* **2010**, *14*, 3–12. [[CrossRef](#)] [[PubMed](#)]
31. Blemker, S.S.; Delp, S.L. Three dimensional representation of complex muscle architectures and geometries. *Ann. Biomed. Eng.* **2005**, *33*, 661–673. [[CrossRef](#)] [[PubMed](#)]
32. Handsfield, G.G.; Greiner, J.; Madl, J.; Rog-Zielinska, E.A.; Hollville, E.; Vanwanseele, B.; Shim, V. Achilles subtendon structure and behavior as evidenced from tendon imaging and computational modelling. *Front. Sports Act. Living* **2020**, *2*, 70. [[CrossRef](#)]
33. Blemker Silvia, S.; Pinsky, P.; Delp, S. A 3D model of muscle reveals the causes of nonuniform strains in the biceps brachii. *J. Biomech.* **2005**, *38*, 657–665. [[CrossRef](#)]
34. Handsfield, G.G.; Inouye, J.M.; Slane, L.C.; Thelen, D.G.; Miller, G.W.; Blemker, S.S. A 3D model of the Achilles tendon to determine the mechanisms underlying nonuniform tendon displacements. *J. Biomech.* **2017**, *51*, 17–25. [[CrossRef](#)] [[PubMed](#)]
35. Wilke, J.; Schleip, R.; Yucesoy, C.A.; Banzer, W. Not merely a protective packing organ? A review of fascia and its force transmission capacity. *J. Appl. Physiol.* **1985**, *124*, 234–244. [[CrossRef](#)] [[PubMed](#)]

**Disclaimer/Publisher’s Note:** The statements, opinions and data contained in all publications are solely those of the individual author(s) and contributor(s) and not of MDPI and/or the editor(s). MDPI and/or the editor(s) disclaim responsibility for any injury to people or property resulting from any ideas, methods, instructions or products referred to in the content.